MEng in Product Innovation Engineering

Master Thesis

Modelling, Control and Performance Evaluation of a Single-Axis Compliant Nano-Positioning System

Supervisor at University of Padova:
Prof. Alberto Trevisani

Co-supervisors at University College of Cork:
Dr. Guangbo Hao
Dr. Richard Kavanagh

Author: Riccardo Sandon

Academic year 2016-2017

Contents

Acknowledgments

I would like to express my sincere gratitude to Dr. Richard Kavanagh and Dr. Guangbo Hao for the continuous support during my master thesis in UCC and for providing me the opportunity to participate in an international conference to present the work done.

Sincere thanks also to Prof. Alberto Trevisani. His guidance helped me during all the time of my research project and in writing this thesis.

I would like to thank also all the components of my family for their patience and help. A particular thank to my mother who supported me spiritually and economically during all my studies with her love and strength.

Finally, I would like to thank all my friends who have been part of this life path for sharing with me a word of encouragement or a listening ear.

Abstract

This thesis presents the results from a preliminary activity devoted to the implementation of high-performance controller for a single axis compliant nano-positioning system. Preliminarily, this work discusses the mechanical design of the system, its peculiar features, and presents a system transfer function that can be used in the controller synthesis. This mechatronic system is designed to achieve nano-motion performances, defined by a precision close to 10 nm. The system layout involves a controller board, a driver, a voice coil actuator, a compliant structure, an optical linear encoder and an aluminum frame. A detailed description of the components and the connection between them is provided. A compliant mechanism is used because, compared to rigid body mechanisms, it has several peculiar advantages (e.g. high precision, no backlash and friction). A voice coil actuator, which has no backlash thanks to its design, is employed to provide excellent position accuracy. The controller is implemented using dSPACE. The stiffness of the compliant mechanism is studied using both theoretical and experimental methods. The logarithmic decrement method is used to estimate the system damping factor. After a detailed description of the design, the thesis discusses both theoretical and practical aspects of three control techniques used for the implementation of a high-performance controller for the nano-positioning system. The control schemes employed to achieve high-precision position control are a PID controller tuned with Ziegler & Nichols methods, a force feedforward controller based on inverse

dynamics and a combination of the PID controller and a force feedforward controller used to achieve higher bandwidth regulation. Control performances are investigated by analysing the capability to track quintic polynomial trajectories. The performances of the control system are analysed focusing on resolution, accuracy and repeatability defined in the standard ISO 9283.

Chapter 1

Introduction

Since the first robot application, continuous improvements in robot precision, re-configurability and speed have been achieved. Nowadays, it is possible to design robots suitable for tasks ranging from large scale manipulation to micro/nano positioning. Currently the application of the robot can be classified as following [1]:

- Industrial robots – Typically articulated arms created for industrial applications such as material handling, painting, welding, etc.
- Domestic or household robots – Used at home, they consist of different type of tools that help with household tasks for example pool cleaning, sweeping, vacuum cleaning, etc.
- Medical robots – This type of robot are employed in medicine environment. Especially, they are used for surgical treatment.
- Service robots – Robot do not included in the other classification
- Military robots – Robots used for military and armed scopes such as bomb discarding, various shipping, and exploration drones.
- Entertainment robots – As a wide-ranging category, they could be model robots such as Robosapiens, heavy weights robot like articulated robot arms employed as movement simulators.
- Space robots – Robots employed in space are used to substitute astronauts in order to do work in dangerous environments, routine procedures like video capture, etc.

- Hobby and competition robots – Robots that is created by student prepared merely for learning, fun and sometimes for contests.

A nano-positioning system is a robotic/mechatronic motion system capable of nanometric motion quality [2]. This is typically defined by an accuracy of better than 10 nm. Currently, most of the positioning systems available are provided by PZT actuator and they achieve high precision performance [3], but small range of motion up to micrometric motion. Nano-positioning systems are often involved in the bio-medical industry, in which its high nano-performance is required for some procedures such as manipulation and analysis of cells [4]. Among all, another relevant area is the Fast Tool Servo (FTS) [5] in which a large amount of research effort has been devoted to improving it (eg. enhancing the trajectory tracking accuracy, increasing motion stroke and bandwidth).

Recently, compliant mechanisms (CMs) have become an increasingly active research topic thanks to the new technologies available which enable the design of manipulators even able to generate displacements with nano-motion quality. The advantages of CMs include [6]: reduction of the number of parts required, reduction of manufacturing and assembly time and costs, enhancement of mechanism precision, no backlash, elimination of wear and lubrication problems due to the removal of mechanical joints, stored energy in the form of strain energy in the flexible members, reduction in weight (significant factor in aerospace and other high performance applications) and ease of miniaturization of MEMS. Thanks to their merits, compliant mechanisms have several high precision applications such as nano-manipulation [7], micro-assembly [8], bio-medical devices [9], minimally invasive surgery [4], micro electro-mechanical systems (MEMS) [10] and fast tool servos [5].

The nano-positioning system presented in this thesis, which exploits a compliant design, is designed to provide nanometric performance over a relatively large range of up to 1mm. Due to the typically nonlinear behavior of CMs, the motion range studied in this paper is restricted to

± 0.2 mm in order to assure a linear response. Such a range is still large with respect to the nanometric precision assured by the system. Stiffness calculation has been carried out using both analytical and experimental method and the linear behavior over the range considered has been demonstrated. Additionally, a linear viscous friction coefficient has been inferred experimentally, to match the under damped free response of the system.

This work is based on a project which has the aim to develop a 3 degrees of freedom (i.e. three translations) nano-positioning system. Only one of the three DOF is studied in this thesis because the three output translations of the CM employed in the system are decoupled from each other. Therefore, three independent control systems can be designed to control the three translations separately, which makes the control system design relatively simple. Moreover, the stiffness and geometrical structures of the CM along the three translational directions are isotropic, so the three independent control systems can be the same. Due to the minimized motion loss between the output displacement of the actuator and the associated output displacement of the CM, both the output displacements of the actuator and the CM can be measured using only one displacement sensor, which further simplifies the control system design [2]. Additionally, the CM has good dynamic characteristics such as large stiffness and low damping factor, therefore, a simple PID controller could be employed to control the system with a high resolution.

The aim of this work is to present closed-loop control schemes guaranteeing high precision motion control. A control system for the nano-positioning device studied must meet strict requirements as follows:

• the system must be capable of operation within a nanometer interval, accurately adjusting to set points within this range of motion;

• the system must exhibit limited overshoot or transient oscillation;

• the controlled displacements must be both bi-directional and cover a large length relative to the desired precision of the controller.

If the objectives outlined are reached, the design may be used in an application as mentioned above which requires nano-motion quality, such as minimally invasive surgery and fast tool servo (FTS), in which it is also required to enhance the trajectory tracking accuracy and increase motion stroke and bandwidth.

This thesis is organized as follows:

- Chapter 2 includes a general introduction of the compliant mechanisms, advantages, disadvantages, application and some aspect of the designing methods. A focus on compliant parallel manipulators (CPMs) has been done because the compliant structure involved is classified into that compliant manipulator category. A detailed description of the compliant mechanism involved is included, with a particular focus on the methodologies used for the stiffness calculation and the damping factor estimate.

- Chapter 3 provides an overview of the nano-positioning system. It introduces all its components and the connection between them. The system transfer function is also obtained, as being an essential preliminary step to design effective control schemes.

- Chapter 4 includes a detailed description of the control schemes and a characterization of the synthesis methods. Firstly a PID control is synthesized using Ziegler-Nichols heuristic method. Secondly, a force feedforward open-loop scheme has been designed based on Newton's law. Finally, a combination of the two control schemes mentioned above has been realized to improve the overall performance of the system.

- Chapter 5 shows experimental results through trajectory tracking and performance analysis. Performance evaluation has been carried out in terms of resolution (minimum incremental solution), accuracy (lack of error) and repeatability along the given linear motion range (± 0.2 mm) in both position and path analysis. Identification, compensation and elimination of a system deadband have been demonstrated at the

end of the chapter. It is shown how the strict clearances of the voice coil actuator previously affect the control system and the improvements resulting from this.

- Chapter 6 gives concluding remarks.

Chapter 2

Compliant Mechanisms

This chapter introduces some relevant aspects of compliant mechanisms (CMs) such as advantages, disadvantages, applications and an oveview of the design methods. A particular focus on the compliant parallel manipulators will be included. The description of the CM employed in the nano-positioning system will be performed and a characterization of the CM features will be presented.

A mechanism is a mechanical device designed in order to transfer or transform input forces and displacements into a desired set of output forces and displacements. Both compliant and traditional rigid body mechanisms have the same final purpose explained above, but they achieve it differently. Rigid body mechanisms are assembled with rigid links connected at movable joints [6]. Consequently, the motions are transferred through the operation of the rigid joint and the relative motion between links. However, traditional mechanisms do not allow flexibility of the members and it is considered a characteristic to avoid. Additionally, neglecting friction losses, the energy is conserved between the input and the output. On the contrary, CMs are not assembled, they are composed by a single component designed to perform the objectives by means of elastic deformation of its flexible members rather than rigid joints [2]. When the input force is transmitted to the output, the energy is not conserved during the motion, but it is stored in the form of strain energy thanks to

the flexible members. In some application, they can be used to store and transform energy to released at a later time or in a different way (e.g. bow and arrow system) [6].

As an example, in Fig. 2.1 is shown a gripper designed using traditional rigid body mechanisms and in Fig. 2.2 is shown a gripper using compliant structure based on flexure motion [11]. In both cases, it is reported the opened and closed configuration.
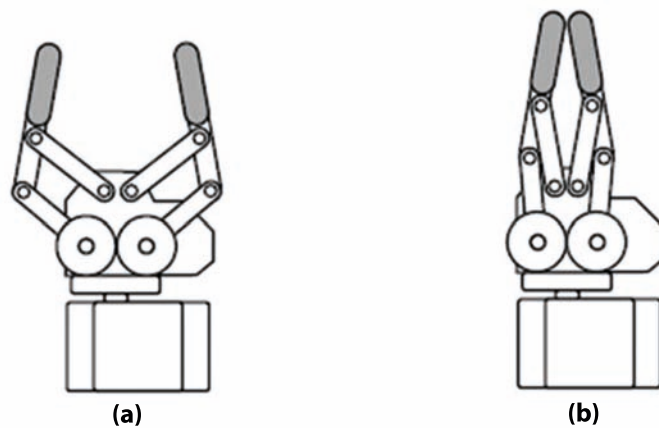

(a)   **(b)**

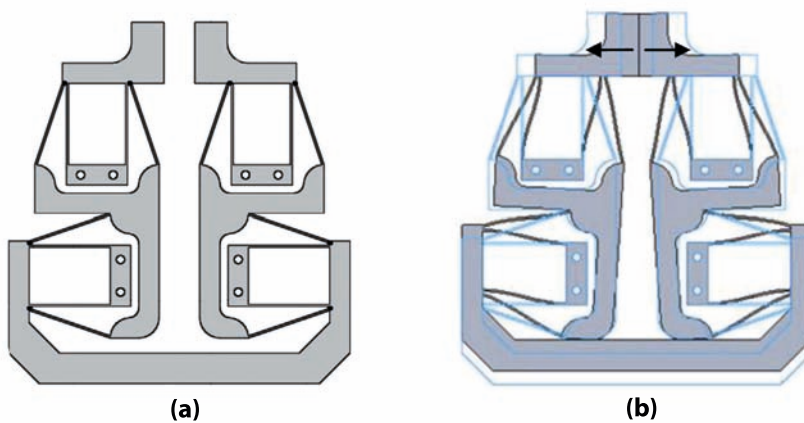**Figure 2.1** Traditional rigid body gripper

(a)   **(b)**

Figure 2.2 Compact distributed compliant gripper

Using CMs, there are some aspects which complicate the analysis, such as parasitic motions and nonlinearities both introduced by large deflections. This is why, in some applications traditional rigid body mechanisms and compliant mechanisms can be combined in partially

16

compliant mechanisms. In [12], it is introduced a method to aid in the design of a class of compliant mechanisms wherein the flexible compliant sections are small in length compared to the relatively rigid body sections.

2.1   Advantages, Disadvantages and Applications

Compliant mechanisms, compared to rigid body mechanisms, have a good number of advantages in their field of work, which is mostly high-precision application. The advantages can be considered in two categories [6]: increased performance and cost reduction. The feature of the compliant mechanisms that reduce the costs is at first the reduced number of parts on the mechanism that, most of the times, is fabricated in a single component. This means that manufacturing, assembly and maintenance costs are dramatically decreased. For the same reason, there is no presence of movable joint, which means reduced wear and need for lubrication. Linked to this, there is increase of the performances and precision due to the reduced number of joints, the eliminated backlash effect and the reduced friction. Generally, they are easy to miniaturize (MEMS) and they are suitable for high hygiene and high precision environment.

Compliant mechanisms present also several disadvantages in some applications. Firstly, the design of CMs requires deep knowledge of mechanism analysis and synthesis methods combined with deflection of flexible members. Secondly, the members are often used with large deflection, which means that the linearized beam equation is no longer valid. Additionally, geometry, material and load-equilibrium equation nonlinearities have to be considered. Thirdly, the energy stored, which has been described as an advantage, sometimes is a disadvantage. E.g. when it is required to hold a certain position for long time, a waste of energy is sustained. Finally, fatigue analysis is an issue for compliant mechanisms

because they are often loaded cyclically and for high temperature application can happen that their fatigue strength limit is too low.

Thanks to their merits, compliant mechanisms have several high precision applications such as nano-manipulation [7], micro-assembly [8], bio-medical devices [9], minimally invasive surgery [4], micro electro-mechanical systems (MEMS) [10] and fast tool servos [5]. The nano-positioning system studied in this thesis, including the CM described afterwards, is a promising candidate for biomedical injection or fast tool servo manufacturing applications.

2.2   Design Methods

As mentioned above, CMs have a good number of advantages and consequently a wide range of applications. Conversely, they need high efforts for the designing and the complexity requires deep knowledge. The general requirements to be considered for the design of a CM are [13]:

- Meet the required number and direction of degrees of freedom (DOF) or degrees of constrain (DOC). The stiffness along the DOC direction should be much larger than the one along the DOF direction.

- Meet the required motion accuracy within the required motion range. In this topic, parasitic motions, which cause lost motion and cross axis-coupling, could be an issue.

- When occurred, meet the stiffness variation along DOF and DOC direction resulting from the displacement changes. A robust control should be design to go against it.

- Meet a monolithic and compact manufacturing.

In general, the process of designing a CM consists of three main steps: synthesis, analytical modelling and optimization. The most used synthesis methods that could be employed to start the design of a compliant mechanism are: (a) parallelogram based approach, method which produces most of the existing compliant translational joint (CTJ) [14]; (b) constrain and position identification based approach, method

that select appropriate constraint elements and identify their locations and orientations. Such selection and identification rely heavily on designers' creative thinking and experience [15]; (c) screw theory based approach; this method can mathematically identify the locations and orientations of the required constraint elements in a compliant mechanism [16]; (d) freedom and constrain topologies (FACT), it represents the theory of the Screw based approach by a library of the most used geometrical shapes [17]; rigid body replacement approach, if a rigid body mechanism already exists, a compliant mechanism can be synthesized by replacing the rigid body mechanism components/joints with the corresponding well known basic compliant mechanisms components/joints [6]. Regarding the second step of the designing process, there are two main approaches to model analytically CMs, one is the free body diagram (FBD) based approach used in [15], and the other is the energy-based approach, using the virtual work principle. The analytical model of a compliant mechanism can be used to proceed with the third step of the designing process, which is the optimization of the geometrical parameters, so that the motion characteristics improve [2]. In this thesis, there will be not a deep study on the design methods, because it is not the main objective. Every references done here is useful in order to explain the complaint mechanism employed in this project.

A tricky behavior of CMs is parasitic motion. Parasitic motion is the difference between the required input motion given on the input stage by the actuator and the effective measured motion of the output stage. Generally, parasitic motion is composed of lost motion and cross-axis coupling [2]. The former represent the difference between an input and an output displacement along a DOF direction, the latter is referred to the motion of a multi-axis output motion stage, in which one DOF direction is affected by the other DOF direction.

Nonlinearity in force-displacement equation is another undesirable aspect of the CMs and it has three sources: material, geometric and load-equilibrium equations nonlinearity [18]. Material nonlinearity occurs

when the deformation of the beams is bigger enough to deform the structure over the elastic region of the equation stress-strain. Geometric nonlinearity arises when the CM is asked to perform large deflections that cause significant changes on the CM geometry (e.g. area, thickness or length) [6]. The nonlinearity of load-equilibrium equations takes into account of the deformed configuration. For this reason, it should be always considered. However, in most of the cases, and also in this project, it is assumed that the analyzed deflections of the CM are smaller compared to the dimension of the structure. Consequently, material and geometric nonlinearities can be neglected since the equation stress-strain can be simplified by linearization in the elastic region and the deformations wideness do not alter the nature of the problem. Regarding the CM analysed in this thesis, it will be demonstrated in Section 2.4.1 that, within the range studied, the force-displacement relation (i.e. the stiffness) could be considered linear.

2.3 Compliant Parallel Manipulators (CPMs)

The parallel manipulator can be defined as a closed-loop kinematic chain mechanism whose end-effector is linked to the base by several independent kinematic chains [19]. They can be classified by according to their nature of motion in three categories: planar, spherical and spatial manipulator. Parallel manipulators are mechanical systems that use more than one chain to support a single platform, or end-effector. The parallel distinction with the serial manipulator is that the end effector is connected to the base by a number of separate and independent linkages working in parallel. These linkages act together, but it is not implied that they are aligned as parallel lines.

The advantages of the parallel manipulator compared with serial one are [20]: high precision, high rigidity, no accumulation of errors due to absence of links, high payload, large moving speed, good compactness,

good dynamics. Conversely, parallel manipulators present some disadvantages comparing with serial manipulator, such as small motion range, fixed actuator mobility, high design complexity.

In addition to all of these characteristics, a CPM, compared with the rigid body version, has all the compliant advantages described above. As an example, the 3RRR parallel manipulator is shown in Fig. 2.3. A scheme of the traditional rigid body 3RRR parallel manipulator has been depicted in Fig. 2.3 (a) and a compliant version of it [21] in Fig. 2.3 (b).
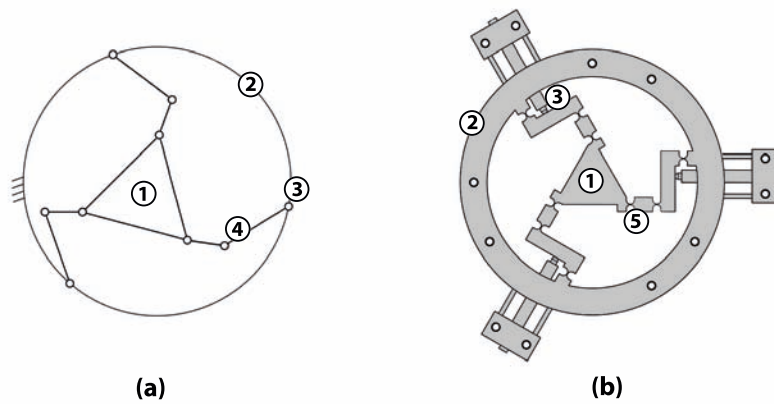

Figure 2.3 3RRR parallel manipulator (a) traditional rigid body version (b) compliant flexure-based version

where the description of the components is as follows: {1} moving platform, {2} stationary frame, {3} actuator position, {4} traditional link and joint, {5} flexure hinge.

CPMs designed for high-precision motion application (i.e. the nanopositioning system studied) have to own the following performance characteristics [22]:

- large range of motion along the desired directions. It is affected by the system size (length and thickness), the material characteristics (σ_s/E ratio) and the conceptual level configuration. A multi-level parallelogram configuration can largely alleviate the significant load-stiffening effect, as showed in Fig. 2.4.
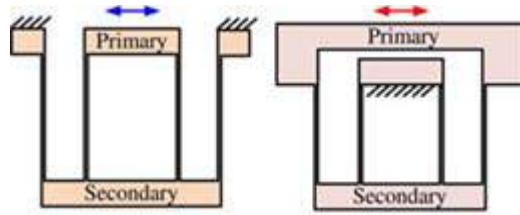
Figure 2.4 Multi-level parallelogram compliant manipulator

- inherently well-constrained lost motion, between actuator input motion and output motion stage; minimal cross-axis coupling in case of multi-axis output motion stage.

- maximal actuator isolation (also input-decoupling, minimal traverse motion of the actuator). Force source actuators (E.g. Voice coil Actuator) typically do not tolerate transverse loads and displacements. Consequently, in the absence of adequate actuator isolation, the actuators have to be connected by means of a decoupler.

- maximal overall stiffness between actuator and motion stage. The increase of the stiffness can be done either changing the geometry of the beams (in width and length) or adding in parallel beams.

- low thermal sensitivities, high compactness, low cost and complexity (easy to manifacture), desired dynamic performance (e.g. high bandwidth).

2.4   CPM Practical Example

The nano-positioning system studied exploits a compliant design in order to perform nano-metric motion. Two main devices compose the CM involved: a Compliant Basic Parallelogram Mechanism (CBPM) (see Fig 2.5) and a XYZ Compliant Parallel Manipulator (CPM) (see Fig. 2.6) [23].

The CBPM part, described in details in [24], transmits mechanical power along a single direction, from the voice coil actuator to an XYZ stage. Basically, it is composed of two BPMs displaced symmetrically. A schematic representation of the CBPM used is reported in Fig. 2.5.
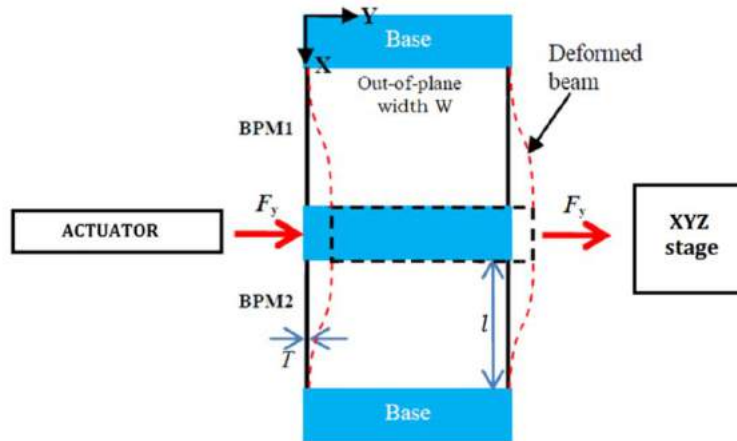
Figure 2.5 CBPM with actual geometry, loading and
displacement indication

Compared to the other parallelogram based compliant translational joints illustrated in Fig. 2.6, the CBPM employed has very good characteristics such as good dynamic, well-constrained parasitic motion, an excellent constraint-based design and good thermal sensitivity [25].
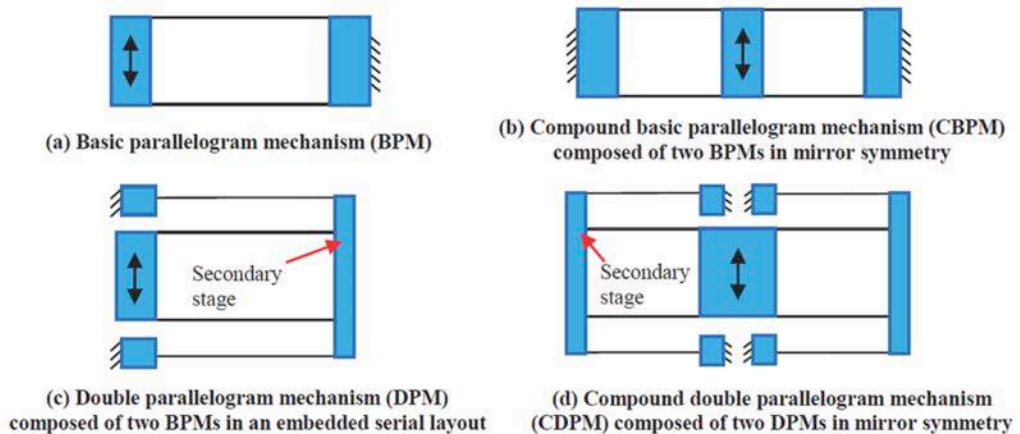

(a) Basic parallelogram mechanism (BPM)

(b) Compound basic parallelogram mechanism (CBPM)
composed of two BPMs in mirror symmetry

(c) Double parallelogram mechanism (DPM)
composed of two BPMs in an embedded serial layout

(d) Compound double parallelogram mechanism
(CDPM) composed of two DPMs in mirror symmetry

Figure 2.6 Four types of parallelogram based compliant
translational joints

The basic parallelogram mechanism in Fig 2.6 (a) is affected by large parasitic translation and slight parasitic rotation along the primary motion. The double parallelogram mechanism and its compound version,

which are depicted in Figures 2.6 (c) and (d) respectively, involve secondary stage to compensate the parasitic translation and rotation, but their stiffness is degraded and the non-controllable secondary mass introduces dynamic issues.

In this context, the CBPM is necessary to sustain the actuator, which cannot be connected directly to the XYZ CPM, as it requires a bigger structure to sustain its weight. It also increases the overall stiffness of the CM to obtain a better dynamic.

The second device of the compliant system involves a fully symmetrical XYZ Compliant Parallel Manipulator (XYZ CPM) described in detail in [7]. It has desirable motion characteristics such as reduced cross-axis coupling and minimum lost motion. A representation of a disassembled XYZ CMP is provided in Fig. 2.7 (a). F_y represents the force coming from the CBPM part. If only one axis is actuated (the Y-axis in this case) 24 beams will contribute to the total stiffness. In Fig. 2.7 (b) the XYZ CPM has been divided in three main parts in order to explain this concept.
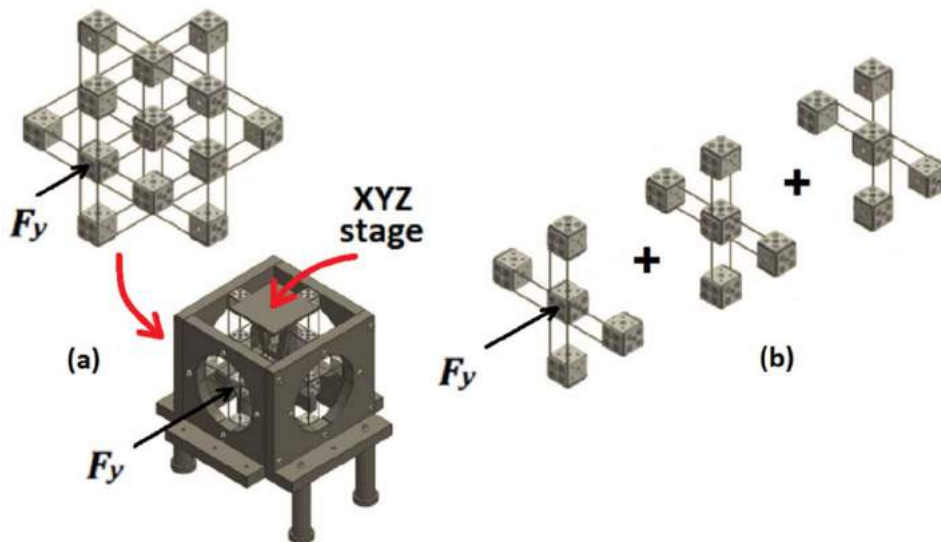

Figure 2.7 The fully-symmetrical XYZ Compliant Parallel Manipulator (CMP) (a) XYZ CMP disassembled (b) beams involved in the degree of freedom (DOF) studied

The XYZ CPM has been designed to provide three DOF with maximal decoupled motion along the three axes. If actuated the all X, Y and Z axes, it isolates traverse motion (motions in the DOC direction) on each axis. If Y-axis is considered, motion along X and Z axes (which represent the DOC directions) are isolated from the input stage of the XYZ CPM (where F_y acts). The actuator (i.e. voice coil actuator) needs maximal isolation from traverse motion due to its strict assembly clearances.

The rigid stages of the XYZ CPM (the external rigid blocks where the input forces are applied) are over constrained by the wire beams, which is good for increasing stiffness in the DOC directions [2]. In order to control the position of the output platform with a closed-loop regulator, the translational displacements should be measured by a three-axis displacement sensor or, more likely, by three independent single-axis displacement sensors, each capable of tolerating the transverse displacements of the output platform. For convenience, in the laboratory prototype, instead of measuring the displacements at the output platform, they are measured at the CBPM part. Indeed, the displacement of the rigid cube linkage is almost the same as the displacement of the output platform because lost motion is negligible. This can be done concurrently along each of the three axes. However, only one axis is studied in this thesis.

Generally, the whole CM has been designed to provide nano-metric performance over a relatively large range of up to 1 mm in both directions. Due to the nonlinear behavior of the CM shown when used over all such a large range, the motion range studied in this thesis is restricted to ± 0.2 mm in order to assure a linear response. However, such a range is still large with respect to the nanometric precision assured by the system. Additionally, as explained above, the three output translations of the CM involved are decoupled from each other. Therefore, three independent control systems can be designed to control the three translations separately, which makes the control system design relatively simple. Moreover, the stiffness and geometrical structures of the CM along the three translational directions are isotropic, so the three independent

control systems can be the same. In this thesis, only one of the three axes is analyzed. Finally, the CM has good dynamic characteristics such as large stiffness and low damping factor. Therefore, also a simple PID controller can be employed to control the system with a high resolution.

2.4.1 Stiffness Calculation

The general single deformed sheet/beam which composes the whole compliant structure studied in this thesis, can be represented as in Fig. 2.8:

Figure 2.8 General single deformed compliant sheet/beam

It is described by the following geometrical characteristics: L is the total length of the beam (x direction), W is the width of the beam (z direction) and T is the thickness of the beam (y direction). Using an analytical linear solution, such as differential method, the stiffness of the single beam can be calculated. With the assumption of small deflection, the Euler-Bernoulli beam equation can be simplified as following:

$$\frac{M(x)}{EI} = \frac{d^2y}{dx^2} \tag{2.1}$$

where:

- $M(x) = F(L - x) - \frac{FL}{2} = \frac{FL}{2} - Fx$ is the total moment

- $I = \frac{WT^3}{12}$ rectangle moment of inertia

- E Young's module

Substituting the M(x) expression on the Euler-Bernoulli beam equation, the vertical displacement law depending on the force F and consequently the stiffness of a single beam, can be calculated as follows:

$$y = \frac{FL^3}{12EI} \qquad > \qquad k_{t,beam} = \frac{12EI}{L^3} = \frac{EWT^3}{L^3} \qquad (2.2)$$

The stiffness of the total compliant mechanism will be calculated firstly by analytical method and secondly using an experimental method.

Using Eq. (2.2), which describes the stiffness of a single beam (see Table 2.1 for the meaning of the symbols), the stiffness of the CBPM and the XYZ CPM can be calculated with analytical method. Basically, the calculation is performed multiplying the single beam stiffness found in Eq. (2.2) by the number of in-parallel beams involved in each mechanism and then summing the two stiffness values. The combined contribution is described in Eq. (2.3).

$$k_t = k_{CBPM} + k_{XYZ\ CPM} = 4 \cdot \frac{EW_{CBPM}T_{CPBM}^3}{l_{CBPM}^3} + 24 \cdot \frac{EW_{XYZ}T_{XYZ}^3}{l_{XYZ}^3} \qquad (2.3)$$

Table 2.1 Compliant mechanism geometrical values

Parameter	Symbol	Value	Unit of measurement
Young's Modulus	E	$69*10^9$	Pa
CBPM Sheet Width	W_{CBPM}	0.04	m
CBPM Sheet Thickness	T_{CBPM}	0.001	m
CBPM Sheet Length	l_{CBPM}	0.05	m
XYZ CPM Beam Width	W_{XYZ}	0.001	m
XYZ CPM Beam Thickness	T_{XYZ}	0.001	m
XYZ CPM Beam Length	l_{XYZ}	0.05	m

Using the numerical values collected in Table 2.1, the theoretical global stiffness along a single direction can be found.

$$k_t = k_{t,sheet} + k_{t,beam} = 88320 + 13248 = 101568\ N/m \qquad (2.4)$$

An experimental validation of the stiffness value computed above has been obtained through a devoted test rig comprising calibrated weights on the nano-positioning system. The weights used for the measurement ranged from 0.25 kg to 9 kg in steps of 0.25 kg. As shown in Fig. 2.9 (a), the relationship between the force applied and displacement measured is almost perfectly linear in the range ± 0.2 mm (the corresponding negative part produces same results). Conversely, a non-linear behaviour arising in case of larger displacements is proved in Fig. 2.9 (b). A cubic best-fit equation is the most appropriate approximation over the range to 0.65 mm.
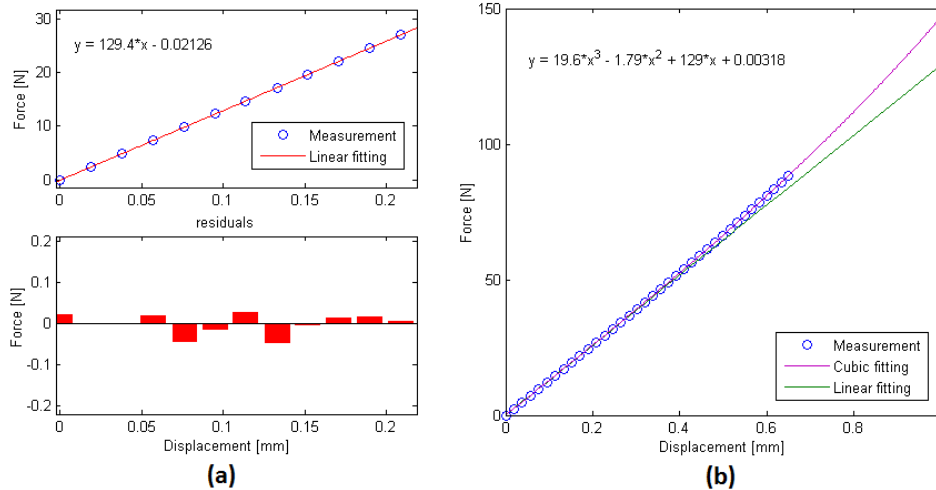

Figure 2.9 Force-Displacement relationship (a) 0-0.2mm range (b) 0-0.65mm range

For the linear region studied in this thesis, the approximately linear function between force and displacement calculated from the experimental method corresponds to:

$$F(x) = 129.4\, x - 0.02126 \tag{2.5}$$

Neglecting the constant part 0.02126 N (which corresponds to an approximate position offset of 0.16 μm), the total stiffness calculated experimentally (CBPM + XYZ CPM) corresponds to 129.4 N/mm.

Such a value is approximately 27% higher than the value calculated theoretically. This is a reasonable result because, for fatigue failure prevention reasons, the beams on the CBPM are designed with a fillet of 3 mm and the beams of the XYZ CPM with a fillet of 1 mm. This reduces the effective length of the beams previously used in Eq. (2.3). As the stiffness of a beam is inversely proportional to the cube of the length, a small decrease of l_{CBPM} and l_{XYZ} will cause a big increase of the total stiffness k_t. Similarly, small errors in the fabrication of the overall compliant mechanism structure could produce big changes on the final value of k_t.

2.4.2   Damping Factor Estimate

The CM discussed above, shows an under-damped behavior with small damping factor (see the sample free response of the system in Fig. 2.10). The logarithmic decrement method is often used to calculate the frequency and damping values from the free vibration response of a single degree of freedom (DOF) system [26]. The technique is simple and provides quick estimates, without the need for extensive computation. The main assumption made is that the transient contains only the response of a single DOF. The method works well for systems with light damping. In this system there is no friction non-linearity and the hysteresis term is very low. Consequently, this method can be used in this system to yield the damping factor.

The system has been excited with an input using a proper tool to give a hit as close as possible to an impulse. The free response of the system in the time domain is shown in Fig. 2.10.
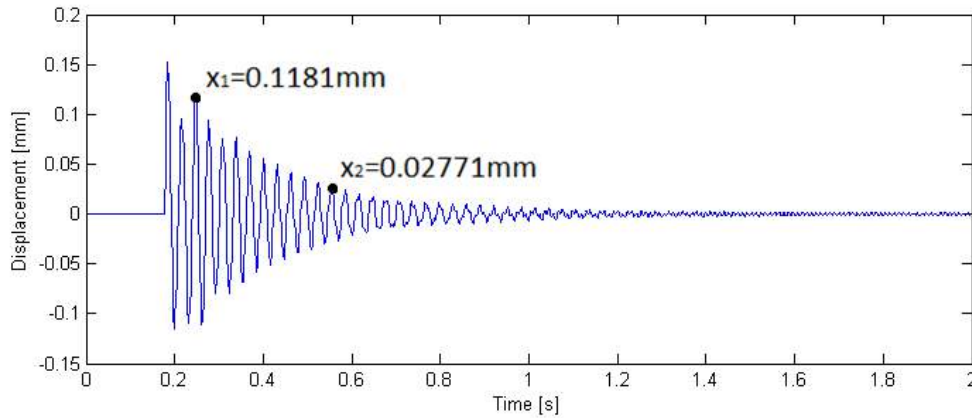
Figure 2.10 Free response of the physical system in the time
domain

Generally speaking, the logarithmic decrement δ is:

$$\delta = \ln\left(\frac{x_1}{x_2}\right) = \xi\,\frac{2\pi}{\sqrt{1-\xi^2}} \qquad \textit{when } \boldsymbol{\xi \ll 1} \qquad \delta = \ln\left(\frac{x_1}{x_2}\right) = \frac{2\pi}{\xi} \qquad (2.6)$$

where x_1 and x_2 are two consecutive peaks and ξ is the damping factor. In order to achieve a sounder estimate of a damping factor, peaks spaced by more than one period are considered. If n=10 is the number of periods between the two peaks, the damping factor ξ can be calculated as follows:

$$\xi = \frac{\ln(x_1/x_2)}{2\pi n} \qquad (2.7)$$

The experimental values obtained for the system is $\xi = 0.023$.

Chapter 3

Nano-Positioning System

Since the first robot applications, continuous improvement in robot precision, re-configurability and speed have been achieved. Nowadays, it is possible to design robots suitable for tasks ranging from large-scale manipulation to micro/nano positioning. A nano-positioning system is a robotic/mechatronic motion system capable of nanometric motion quality [2]. This is typically defined by an accuracy of 10 nm.

The laboratory prototype of the nano-positioning system presented, which exploits the compliant design described in Chapter 2, is shown with a labelled photograph in Fig. 3.1. It has been designed to perform nanometric motion over a range of up to 1mm. Due to the demonstrated nonlinear behavior of the compliant structure, the motion range studied in this thesis is restricted to ±0.2 mm in order to assure a linear response. Such a range is still large with respect to the nanometric precision assured by the system. As described in Chapter 2, only one of the three axes has been analyzed. If one of the three axes can be controlled performing nanomotion quality, the control scheme can be equally replicated on the other two axes. This is due to the decoupled motion of the three axes and to the isotropic stiffness and geometrical structures of the CM along the three translational directions.
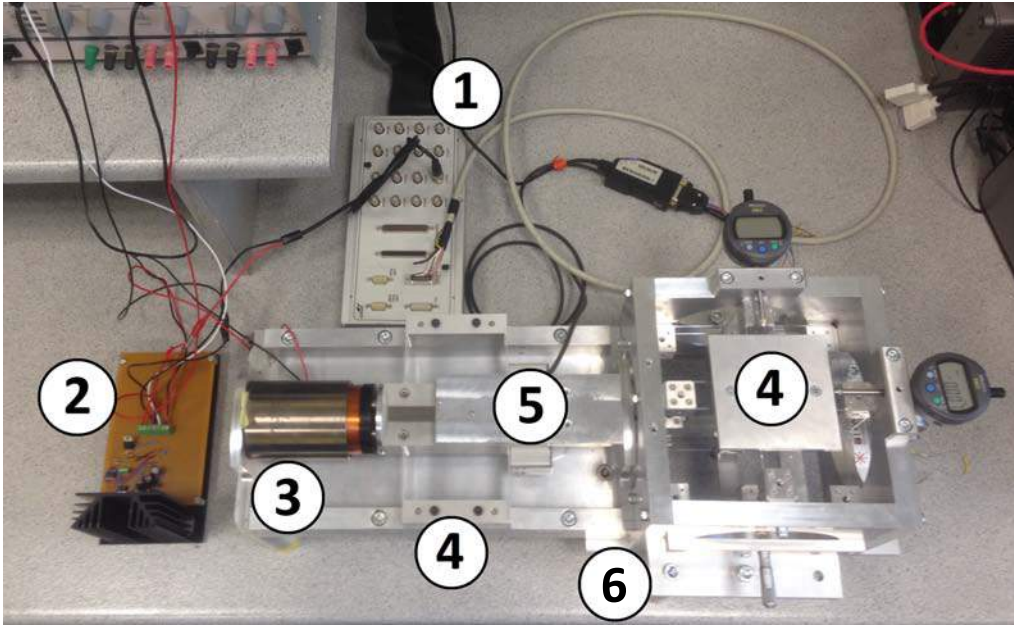
Figure 3.1 Nano-positioning system (1) dSPACE DS1004 (2) Operational Amplifier OPA 549 (3) Voice Coil Actuator LA30-48-000A (4) CBPM + XYZ CMP Compliant Mechanism (5) Linear Optical Encoder (6) Aluminum frame

There follows a description of the physical components using the numbers of the Fig 3.1 as references:

1. A Digital Signal Processor (DSP) dSPACE DS1104 board upgrades the PC to a development system for Rapid Control Prototyping (RCP). The control model can be designed using Simulink, the simulation can be run on the dSPACE DS1004 board via Simulink Coder, and subsequently a Graphical User Interface (GUI) can be designed using dSPACE ControlDesk to observe the results and modify the model parameters. Among all the dSPACE connectors, a 16 bit Digital to Analog Converter (DAC) output and an incremental encoder connector have been used. The output from the DAC is a voltage signal in the range $\pm$ 10 V.

2. A high-current, high-voltage operational amplifier (OPA 549) based circuit provides the current loop controller required to supply the voice coil actuator with the necessary current.

3. A voice coil actuator (VCA) LA30-48-000A from BEI Technologies INC applies to the compliant structure a force $F(t)$ proportional to the current $i_{act}(t)$ coming from the driver. The VCA is simply composed of a permanent magnet and a coil. The air gap between the two part enables frictionless and cog-free actuation

4. The compliant mechanism, which is composed by two main parts, has been described in the previous chapter.

5. A Linear Optical Encoder SI-HN-4000-01-0-FN-403-003-3 from Renishaw plc with read head number SR015A provides position feedback with $5nm$ resolution, so that, it enables a closed loop control.

6. An aluminum frame supports the voice coil actuator, the compliant structure and the linear optical encoder. It has been subjected to a vibrational study for reducing environment vibrational disturbances from ± 150 nm to ± 30 nm approximately.

A block diagram of the system is provided in Fig. 3.2: it shows all the components involved and the connection between them.
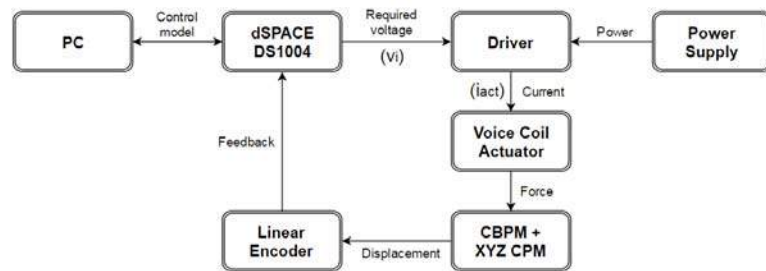

Figure 3.2 System block diagram

Detailed descriptions of the components of the system and the open loop system transfer function have been carried out in the following part of this chapter.

3.1 Digital Signal Processor dSPACE DS1104

The dSPACE DS1104 Controller Board upgrades a PC to a development real-time system for rapid prototyping control (RPC). The real-time hardware based on PowerPC technology and its set of I/O interfaces make the controller board an ideal solution for developing controllers in various fields, such as drives, robotics, and aerospace. [27]. Specific interface connectors panel shown in Fig 3.3 provides easy access to all input and output signals of the board.

Figure 3.3 dSPACE DS1104 controller board: connectors panel

The connectors available in such a controller board are:

- Analogue to Digital input converter with 16 bit resolution multiplexed to 4 channels (ADCH1-4).
- 4 Analogue to Digital in-parallel input converters with one channel each (ADCH5-8).
- 8 Digital to Analogue output converters with a 16 bit resolution (DACH1-8).
- Digital I/O connector.
- I/O Slave DSP digital connector.
- 2 independent digital incremental encoder interface.
- 2 single UART serial interface connectors.

The connectors used for this project are highlighted in Fig. 3.3. Firstly, the DACH1 output connector, with a 16 bit resolution, converts the digital voltage signal coming from the control model to the analogue voltage signal going to the driver. The dSPACE board DACH connectors have maximum output range ± 10 V. Since, during the D/A conversion, the dSPACE board multiplies the input signal by 10 times, the PC model output signal should be within the range ± 1 to obtain an analogue signal included in the maximum range ± 10 V. For this reason, a gain 10^{-1} will be necessary before the "DAC" block on the control model. Secondly, a digital incremental encoder interface has been used to acquire the position feedback signal from the encoder, so that, a closed loop control can be designed. It has 24 bit resolution and selectable single-ended (TTL) or differential (RS422) input.

After the physical connections, the control model can be designed using Simulink. Real-Time interface provides Simulink blocks for graphical configuration. The DS1104 Simulink blockset, shown in Fig. 3.4, has to be used into a Simulink block diagram for the communication between the PC and the controller board.
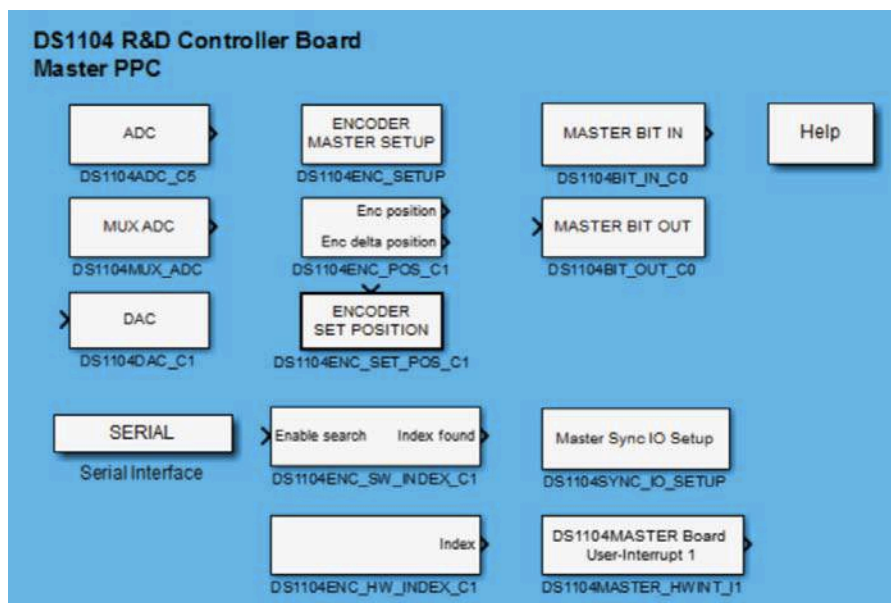

Figure .3.4 DS1104 Master PPC Blockset

Among all, the "DAC" block has to be used to receive the voltage signals commanded from the Simulink model and send them to the DACH1 connector. Instead, the digital incremental encoder interface needs two blocks: "ENCODER MASTER SET UP" and "Enc position/Enc delta position" blocks. The former sets the global parameters of the channel and it is necessary to use any other encoder block from the Simulink library. The latter reads the position signal from the physical device.

Once the Simulink model is designed, the corresponding code can be generated via Simulink Coder simply clicking Ctrl+B and, having used the real-time interface, downloaded on the DS1104 R&D Controller Board. The main advantages of this automatic code generation are: firstly, the Simulink model is ready to be compiled and it is not necessary to convert it in another programming language; secondly, the generated code does not need to be downloaded and implemented on the dSPACE hardware, it is done automatically. If errors occur on the compilation, they can be detected observing the Matlab workspace, in which all the operations carried out by the compiler can be analysed.

At this point, the model created and downloaded on the controller board can be used for carrying out measurements on the physical system. The dSPACE ControlDesk software, described in [28], allows a real-time communication between the PC and the controller board with the purpose of observing the results and varying the model parameters. It offers many fundamental features for experiments creation and management. With dSPACE ControlDesk, project/experiment data (such as layouts, data sets, and measurements) can be prepared for later use in the operator mode or in ControlDesk using a Graphical User Interface (GUI). A layout example of the ControlDesk interface is shown in Fig. 3.5 in which the main sections have been outlined using numbered label.
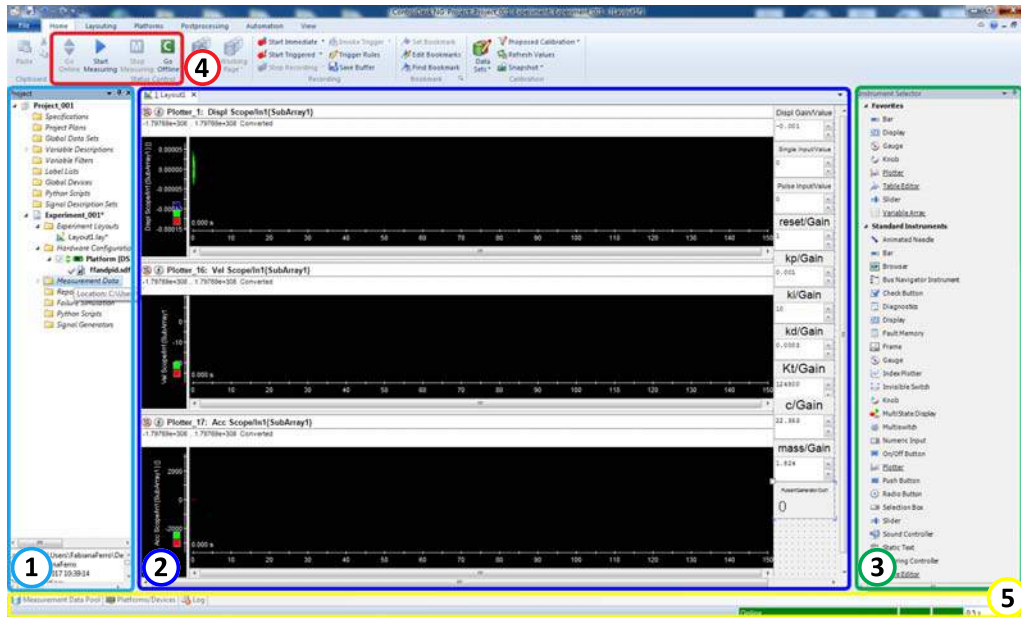
Figure 3.5 ControlDesk layout example

All the functions of this prototyping system are countless. In the following discussion, only the functions, divided by sections, actually used in the project are explained:

1. Navigator panel. It incorporates different subsections to organize layouts associated to different experiments, to manage the folders included in a project (e.g. measurements data, hardware configuration, variable description) and to describe the instrument of the visualized layout.

2. Work area. It is the graphical area available to create layout to communicate with the code implemented on the dSPACE controller board. It is composed by the instruments selected from the intrument selector area. By drag & drop, each variable that need to be controlled can be connected to the assigned instrument.

3. Instrument selector. It includes all the instruments necessary for observing the results and varying the parameters of the project in Real Time dealing directly with the dSPACE board. The instruments can be placed on the layout by drag & drop and then configured or linked to the variables interested. Among all, the most used instrument for this project are the Plotter, which is useful to control every signal trend

(e.g. input and output signals, but also specific values of the model, such as PID separate contributes trend) and the Numeric Input, which is necessary to change the values of the key parameters, such as the PID gains, the Starter Input signal and the Displacement gain.

4. Measurement control. It is situated on the top of the window and it allows the user to go online and offline with the platform and to start and stop the measurement.

5. Tool window. This section shows error messages, enables to manage the model variables included in the .sdf file generated by the Simulink Coder and allows the drag & drop loading of the variables into the layout.

Finally, when the measurements are carried out, they can be saved and exported in Matlab format (i.e. .mat) and the results can be analysed using all the mathematical, graphical and statistical instrument of Matlab.

3.2   Driver

The driver is based on an operational amplifier OPA 549 based circuit which allows the analogue voltage input to control the current flowing in the actuator using a sense resistor [29]. Since the signal from the dSPACE is limited between $\pm 10\,V$, the bidirectional movement of the actuator can be achieve with a simple driver circuit. Additionally, this driver is designed to be able to provide the current necessary to reach the compliant mechanism maximum displacement (i.e. ± 1 mm). The circuit of the driver is composed by three main parts as shown in Fig. 3.6: (a) a voltage divider, (b) a buffer to isolate the two circuit elements and (c) voltage to current converter. Moreover a heat sink has been embedded to dissipate the heat being produced by the high current owing in the circuit. This heat sink is 125mm×88mm×30mm in size and has a thermal resistance of 2.2 °C/W.
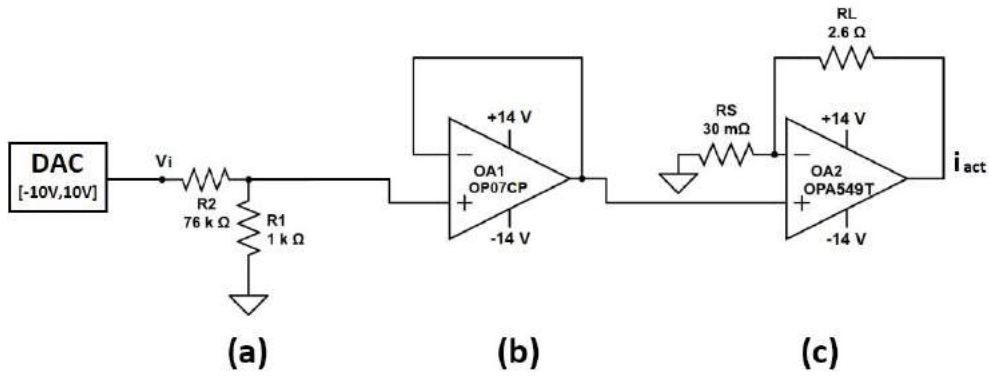
Figure 3.6 Driver circuit (a) voltage divider, (b) buffer (c) voltage to current converter

where v_i is the input analogue voltage signal coming from the dSPACE DACH1 connector, R_1 and R_2 are the two resistances which compose the voltage divider, ± 14 V is the voltage provided by the power supply, R_L is the load resistance (actuator DC resistance), R_S is the sence resistor needed to control the current with a current loop, i_{act} is the current flowing through the coil of the actuator.

The relation between the input voltage signal $v_i(t)$, coming from the controller board, and the output current $i_{act}(t)$, going to the actuator coil, has to be calculated. The driver gain k_d can be found analysing the circuit in Fig. 3.6. The relation between the input voltage signal $v_i(t)$ and the voltage signal after the voltage converter $v_+(t)$ is explained in Eq. 3.1 and the two voltage values $v_+(t)$ and $v_-(t)$ can be considered equal. Then, the current flowing in the sense resistance is equal to the current flowing in the load resistance and, using Ohm's law, $i_{act}(t)$ can be expressed as $v_-(t)$ divided by R_S (see Eq. 3.2).

$$v_+(t) = v_-(t) = \frac{R_1}{R_1 + R_2} v_i(t) \tag{3.1}$$

$$i_{act}(t) = i_{Rs}(t) = \frac{v_-(t)}{R_S} \tag{3.2}$$

Substituting $v_-(t)$ in Eq. 3.2, the relation between $v_i(t)$ and $i_{act}(t)$ (i.e. k_d) has been calculated in Eq. 3.3 and, using the values reported in Fig. 3.6, its value has been found equal to k_d=0.4329 A/V.

$$i_{act}(t) = \frac{R_1}{R_1 + R_2}\frac{v_i(t)}{R_s} = k_d v_i(t) \tag{3.3}$$

The open loop current response of the driver to a 2A step signal has been measured in order to understand if the driver can be considered ideally as a gain or, conversely, some other dynamics do not allow to have the amount of current required instantly. The signal given as an input from the dSPACE ControlDesk (required current) has been compared with the output current flowing through the actuator coil (actual current) in Fig. 3.7. In order to measure the output signal, a current probe with 0.05 A resolution has been used and connected on the dSPACE board into an Analog to Digital converter.
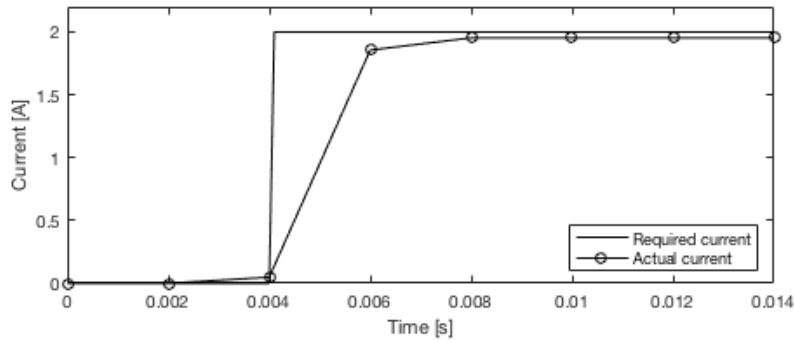

Figure 3.7 Required current VS Actual current (2A step, 2.5ms delay)

It can be seen that the required current is provided within the sample time used for this study (i.e. 0,002 s). Additionally, less than 2 A is necessary to achieve the bidirectional movement ±0.2 mm. Therefore, the driver is able to provide current promptly to the actuator within a sample time and it is not considered as a reason of delay under our assumptions.

3.3   Voice Coil Actuator

The actuator employed on the nano-positioning system is a voice coil actuator (VCA) LA30-48-000A from BEI Technologies INC [30] illustrated in Fig. 3.8 (a). The traditional architecture of a VCA is shown in Fig. 3.8 (b).
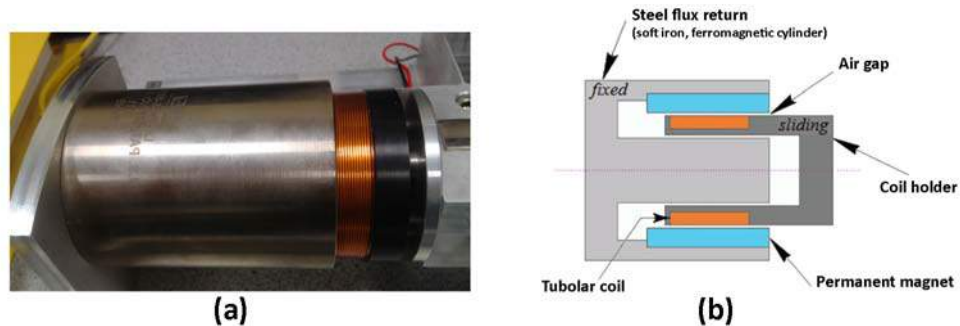

Figure 3.8 Voice Coil Actuator (a) LA30-48-000A BEI Technologies INC (b) VCAs traditional architecture

VCAs operate via the Lorenz force phenomenon, using the interaction between a current-carrying coil, which is the moving part attached on the compliant mechanism that generates the movement, and a permanent magnet (radially oriented magnetic field), the stator, that is fixed on the aluminum frame. The basic principle, with which the VCAs work, expresses that if a current-carrying conductor is placed in a magnetic field, a force will act upon it. An inner core of ferromagnetic material set along the axial centerline of the coil is used to complete the magnetic circuit. The force generated axially upon the coil, when current flows through the coil, will produce relative motion between the parts [31]. The best peculiarities of a VCA are given by its physical design that enables non-contact, frictionless and cog-free actuation. This provides a high-resolution component with high position accuracy.

On the nano-positioning system studied, the coil is directly assembled on the compliant structure. So that, when the current flows through the coil, the force $F(t)$ acts directly to the compliant structure.

$F(t)$ is proportional to $i_{act}(t)$ by the force sensitivity factor ($k_f = 35.14 \, N/A$) as described in Eq. 3.4.

$$F(t) = k_f \, i_{act}(t) \qquad (3.4)$$

The VCA employed in this project has the following features:

- Peak force 445 N
- Continuous stall force 133.8 N
- Stroke 12.7 mm
- Max theoretical frequency 34.5 Hz
- Clearances on each side of the coil 0.51 mm
- Weight of the coil 0.744 kg
- Weight of the field 2.25 kg

The clearances mentioned above are very strict criteria to be respected, otherwise the performances of the VCA dramatically decrease.

3.4 Compliant Structure (CBPM + XYZ CPM)

The compliant structure employed has been deeply described in Section 2.4. It is composed of two devices: a Compliant Basic Parallelogram Mechanism (CBPM) and a XYZ Compliant Parallel Manipulator (CPM). The features of this CM are summarised below:

- Overall stiffness $k_t = 129460$ N/m
- Damping factor $\xi = 0,023$
- CBPM mass $m_{CBPM} = 0,9$ kg
- XYZ CPM mass $m_{XYZ} = 0,18$ kg

3.5 Linear Optical Encoder

A linear optical encoder produced by the company Renishaw plc (model number SI-HN-4000- 01-0-FN-403-003-3, readhead number SR015A) has been selected to read the position of the manipulator and obtain a closed-loop control. It provides high speed positional feedback with a 5nm resolution [32]. This encoder is composed of a scale, which is installed on the compliant structure (moving platform), and a readhead that reads the position from the scale. The readhead is fixed on the aluminum frame through a support accurately manufactured and studied. The support has to allow a correct positioning of the readhead to respect the strict installation tolerances (see references highlighted in Fig. 3.9). The readhead reads the encoded position from the scale and converts it into a digital or analogue signal. This signal is then processed and decoded in the microprocessor for use in feedback.
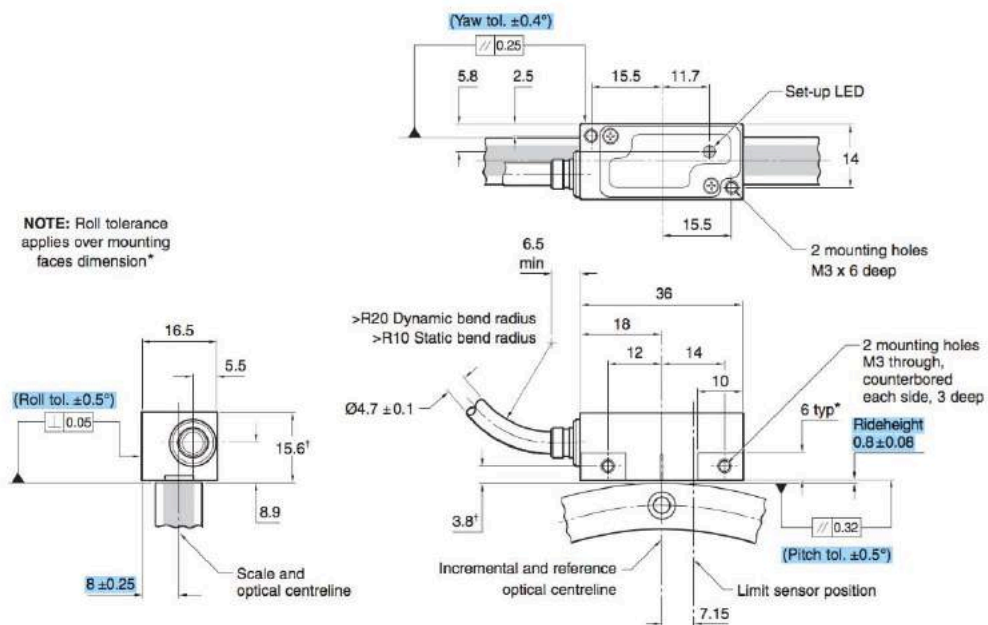

Figure 3.9 SiGNUM Renishaw Encoder installation drawing

To verify if all the tolerances are respected, the SIGNUM software interface, provided by Renishaw, can be used to check the strength of the

signal and the readhead pitch status. Once the encoder has been installed correctly, taking into account of every tolerance, it has to be calibrated always using its dedicated software. More info about calibration and signal strength can be found in the SIGNUM software user guide [33]. This software can be useful also for other functions, such as switching on/off the automatic gain control, using the reference mark display or a digital read out display.

3.6   Aluminum Frame

The aluminum frame supports the voice coil actuator, the compliant structure and the linear optical encoder (see Fig. 3.10). Its weight including all the components installed is approximately 25 kg and it is well distributed in 6 feet.
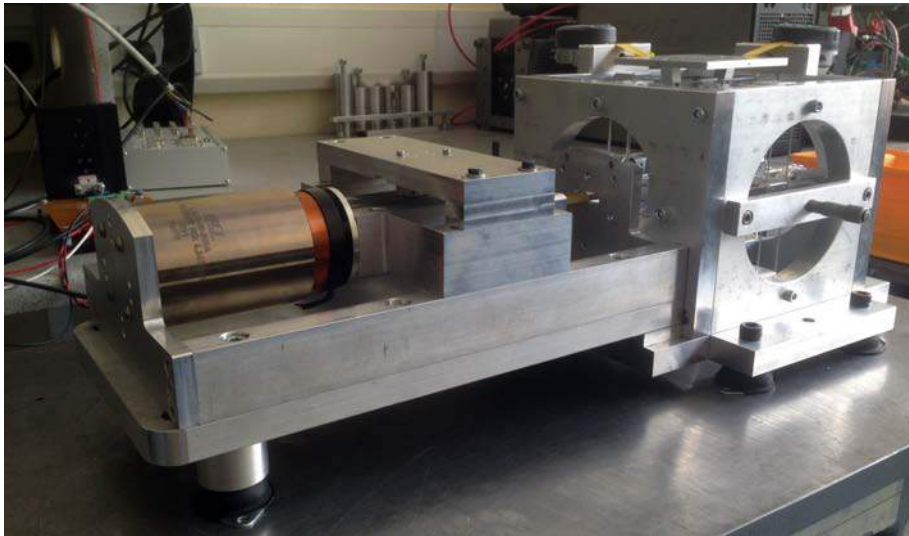

Figure 3.10 Final aluminum frame

Initially, the frame was provided of 6 relatively long legs and it had no anti-vibrational mounts. Since nanomotion quality is required, vibration on the mechanism had to be reduced as much as possible whitin the range ± 10 nm. A vibration measurement has been carried out with the initial condition as described above and the results are shown in Fig. 3.11.

Vibrations on the system were in a range of approximately ± 100 nm. Additionally, a vibration frequency of 40Hz has been recorded.
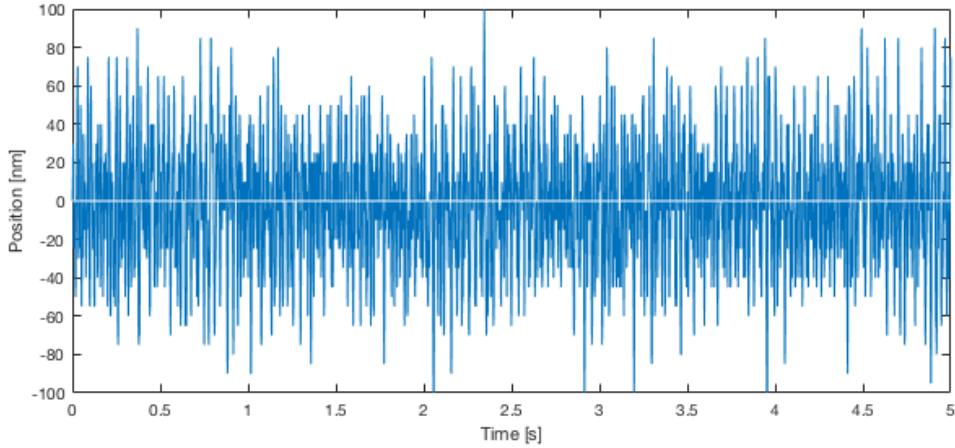

Figure 3.11 Vibration analysis: initial condition

It is clear that this range of vibrations did not allow to obtain a nano-motion quality and it had to be reduced. For this reason, two adjustments have been done on the system: firstly, suitable anti-vibrational feet have been installed on each leg; secondly, the length of the legs has been reduced as much as possible since they acted as cantilevers in the direction of the displacement measured.

The mount installed on the system is DSD 40 with shore 60 Sh produced by AMC. It has been chosen taking into account the characteristics of the system, the frequency of the vibration and the elastic property diagram found in its technical sheet [34]. Illustration of the mount has been inserted in Fig. 3.12 (a) and part of the elastic property diagram has been reported in Fig. 3.12 (b). The total mass of the system is approximately 25 kg and is well distributed on 6 legs, so that, on each leg acts a mass of 4,2 kg. Following general rules, the natural frequency of the mounts chosen has to be half, or less, of the frequency of the vibration detected. Then, the natural frequency of the mounts should be 20 Hz, or less. Consequently, the best suitable mount is DSD 40 (60 Sh), highlighted in Fig. 3.12.

Figure 3.12 DSD 40 (60 Sh) anti-vibration mounts produced by AMC
(a) Geometric representation (b) Elastic property diagram

After installing the mounts and adjusting the legs of the frame, the new vibration range has been estimated with a new test. The results in Fig. 3.13 show that the amount of the vibration has been reduced to a range of approximately ± 35 nm, by 60% compared to the initial measurement, which is a good starting point to achieve nano-motion performances.

Figure 3.13 Vibration analysis: after adjustments

An additional plot is needed to show the amount of the vibration after the adjustments and turning off the power supply (see Fig. 3.14). A range of approximately ±10 nm has been detected, which means that the mechanical vibrations from the floor have been almost completely eliminated. Another amount of vibrational noise from the electrical part of the system (i.e. driver) has been found to affect the measurements. In the future work, a new driver with higher performances could get rid of these disturbances.
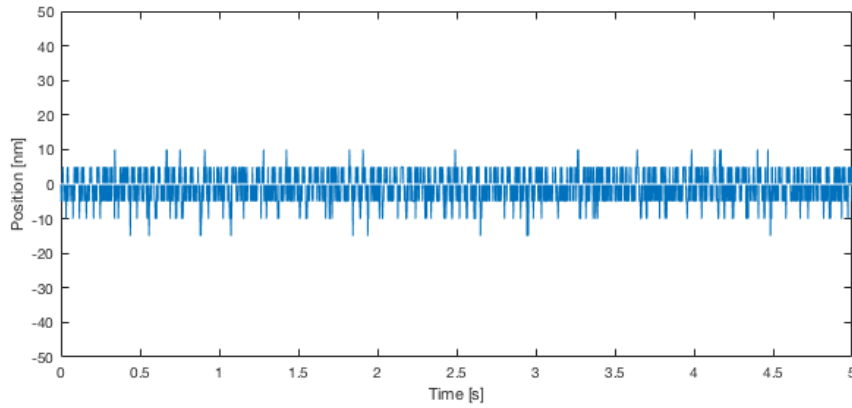
Figure 3.14 Vibrational analysis: after adjustments and power supply off

3.7   System Transfer Function

The transfer function (input: command voltage signal from the dSPACE board; output: displacement of the platform) can be found by using basic model for the system components. Obtaining the transfer function (i.e. a dynamic model of the system) is an essential preliminary step to design effective control schemes. Merging Eqs. (3.3) and (3.4), the force produced by the actuator $F(t)$ can be considered proportional to the commanded voltage signal $v_i(t)$ provided by the DAC:

$$F(t) = k_f i_{act}(t) = k_f k_d v_i(t) \tag{3.5}$$

Considering Newton's law, the equilibrium of the forces applied on the compliant mechanism can be expressed by the following equation:

$$F(t) = m_{tot}\ddot{x}(t) + c\dot{x}(t) + k_t x(t) \tag{3.6}$$

where m_{tot} is the total mass considering the VCA coil (m_{act}), the CBPM (m_{CBPM}) and the XYZ CMP (m_{XYZ}); k_t is the overall compliant stiffness described in Section 2.4.1; c can be calculated by making use of the damping factor inferred in Section 2.4.2 ($c = 2\xi\sqrt{k_t m_{tot}}$). Merging Eqs. (3.5) and (3.6) gives:

$$k_f k_d v_i(t) = m_{tot}\ddot{x}(t) + c\dot{x}(t) + k_t x(t) \tag{3.7}$$

The Laplace transformation of Eq. (3.7) is:

$$k_f k_d V_i(s) = m_{tot}X(s)s^2 + cX(s)s + k_t X(s) \tag{3.8}$$

Then, the transfer function S(s) between the output $X(s)$ and the input $V_i(s)$ can be found:

$$S(s) = \frac{X(s)}{V_i(s)} = \frac{k_f k_d}{m_{tot}s^2 + cs + k_t} \tag{3.9}$$

Table 3.1 System transfer function values

Parameter	Symbol	Value	Unit of measurement
Driver gain	k_d	0.4329	A/V
Force Sensitivity	k_f	35.14	N\A
Stiffness	k_t	129460	N\m
Damping Factor	ξ	0.023	/
Viscous Friction	c	22.353	$\sqrt{KgN/m}$
Total Mass	m_{tot}	1.824	Kg
Actuator Mass	m_{AC}	0.744	Kg
Translator Mass	m_{Tran}	0.9	Kg
CPM Mass	m_{CPM}	0.18	Kg

Using the numerical values collected in Table 3.1, the calculation of $S(s)$ can be performed in Eq. (3.10).

$$S(s) = \frac{X(s)}{V_i(s)} = \frac{15.21}{1.824s^2 + 22.353s + 129460} \qquad (3.10)$$

In order to analyse the system, a Bode diagram is plotted in Fig. 3.15. The poles of the transfer function and the natural frequency of the system are listed below.

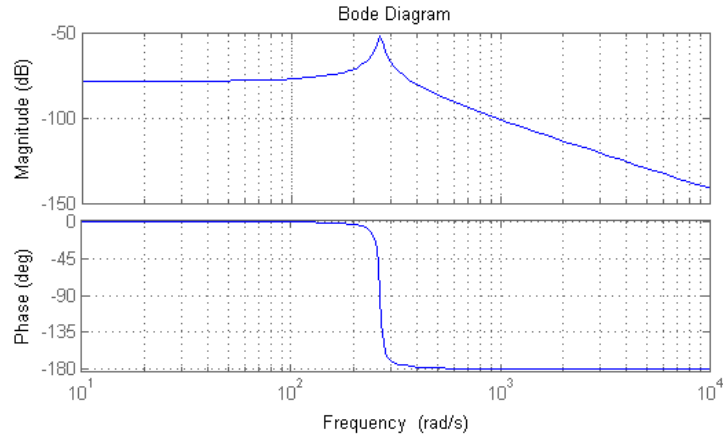$$s_{1,2} = -6.127 \pm 266.343i \qquad \omega_n = 266.413 \; rad \; s^{-1} \qquad (3.11)$$

Figure 3.15 Bode diagram of the system transfer function

An example of open loop trajectory response is plotted in Fig. 3.16 to show the ability of the system to follow the required displacement shown in Fig. 3.16 (a) as well as the corresponding required velocity shown in Fig. 3.16 (b). The results show a micrometer motion quality in both the negative and positive range using only feed forward terms, which is a great starting point for implementing a high-precision closed-loop control. The feed forward input is based on the force calculated making use of Eq. (3.6). The trajectories are computed by quintic polynomial equations.
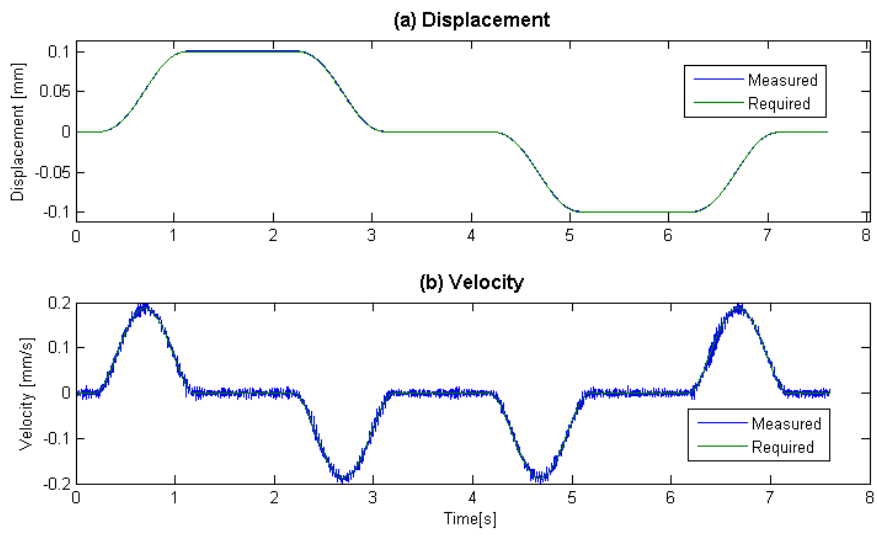
Figure 3.16 Open loop trajectory response (a) Displacement

(b) Velocity

Chapter 4

Control Strategy

This chapter describes some control theories and the regulators synthesized to guarantee high precision motion control of the nano-positioning system studied. Firstly, a PID controller has been designed and the related closed-loop transfer function has been presented. The synthesis of the controller has been performed using the Ziegler-Nichols method. A root locus analysis has been carried out checking the individual contribution of the PID gains and bandwidth estimation has been done using chirp analysis. Secondly, a force feedforward (FF) scheme based on the Newton's law has been implemented to estimate accurately the open-loop system behavior. Finally, the PID controller has then been combined with the feedforward scheme to achieve the best performances in both the transient and in the steady state conditions.

Control schemes for this nano-positioning system must meet strict requirements as follows:

- the system must be capable of operation within a nanometer interval, accurately adjusting to set points within this range of motion;
- the system must exhibit limited overshoot or transient oscillation
- the controlled displacements must be both bi-directional and cover a large length relative to the desired precision of the controller.

If the objectives outlined above are reached, the design may be used in an application which requires nano-motion quality, such as minimally invasive surgery [4] and fast tool servo (FTS) [5] in which it is also required to enhance the trajectory tracking accuracy and increase motion stroke and bandwidth.

From a control point of view, the voltage signal $v_i(t)$ commanded by the controller board represents the input variable which, on the physical system, allows to perform the required displacement $x(t)$ of the moving platform, output variable. The nano-positioning system described in the previous chapter involves a linear voice coil actuator activated by a given current coming from the driver. The amount of force $F(t)$ produced by the actuator is dependent on the given current $i_{act}(t)$, which in turn is proportional to $v_i(t)$. Based on the voltage applied $v_i(t)$, the system transfer function computed in section 3.7 is used to calculate $x(t)$. This transfer function will be used in this chapter for the analysis and synthesis of the controller.

4.1 PID Control

The PID controller is a closed loop feedback controller widely used in a variety of applications. It is well known that it generates an output which is the sum of three terms, respectively proportional to the error between the reference and the output signal by the gain K_P, to its integral by K_I and to its derivative by K_D. The control action produces two effects: one is similar to a feed forward action, while the other depends on the actual state of the system and it modifies the system dynamics [35]. The definition of the system transfer function is essential to reproduce and simulate the behavior of the physical system. By analysing the PID controller in the Laplace domain, its transfer function is:

$$C(s) = \frac{s^2 K_D + s K_P + K_I}{s} = K_P(1 + T_D s + \frac{1}{T_I s}) \qquad (4.1)$$

where $T_I = K_P/K_I$ is the reset time constant and $T_D = K_D/K_P$ is the derivative time constant.

The resultant open-loop transfer function G(s) of the system studied (see Eq. (4.2)) is the product of the system transfer function of Eq. (3.10) and the PID transfer function of Eq. (4.1). Consequently, the closed-loop transfer function $(L(s) = G(s)/(1 + G(s)))$ keeps the form of Eq. (4.3).

$$G(s) = \frac{15.21(s^2 K_D + s K_P + K_I)}{(1.824 s^2 + 22.353 s + 129460)s} \tag{4.2}$$

$$L_{PID}(s) = \frac{15.21(s^2 K_D + s K_P + K_I)}{1.824 s^3 + (22.353 + 15.21 K_D)s^2 + (129460 + 15.21 K_P)s + 15.21 K_I} \tag{4.3}$$
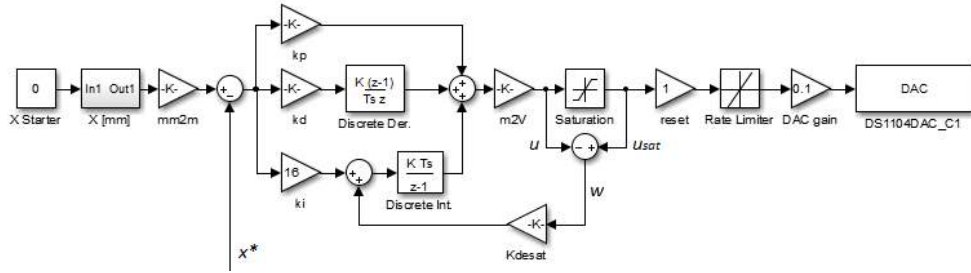
Figure 4.1 PID Simulink model

The Simulink model of the PID control designed is shown in Fig. 4.1. The "X[mm]" block represents a subsystem which, when triggered by the "X Starter" block, reads and reproduces data displacement values from the Matlab workspace. The x* signal is the position feedback from the linear encoder. The driver voltage input $V_i(s)$ is generated by the dSPACE board via the "DAC" block. The "DAC gain" block is necessary to ensure that there is a scaling between the input of the "DAC" block and the analogue output voltage (i.e. if the Simulink signal range is ± 1, the analogue output voltage range is ± 10 V). The conversion from meter to volt is done by the "m2V" gain block. It is based on the $k_{m2V} = 8510$ V/m gain, calculated using Eq. (3.5) and the Hooke's law, as explained in Eq. (4.4).

$$v_i(t) = \frac{k_t}{k_f k_d} \cdot x(t) = k_{m2V}\, x(t) \tag{4.4}$$

The "Saturation" block is a safety block that maintains $V_i(s)$ within the controller limits (set at $\pm 10V$). The "Rate limiter" block is necessary to avoid fast voltage changes that cannot be read by the linear encoder. It responds to changes of at most 0.135 m/s, which can be expressed as 1149 V/s using k_{m2V}.

Introducing saturation on the model corresponds to introduction of a non-linearity. The presence of saturation together with a large integral term could lead to a wind-up non-linear behavior, which degrades the performance of the system. Several techniques can be employed to overcome the wind-up phenomenon, which are all based on the idea of feeding the control system with the saturated signal. The technique used in this paper is back-calculation [36]. The signal $w(t) = u_{sat}(t) - u(t)$ is feedback before the integrator, through a positive gain K_{desat}, which determines the speed of reset in case of saturation. When the system is working linearly, $w(t)$ is null. Otherwise, $w(t)$ has a negative value that helps to reset the integral term.

Ziegler-Nichols heuristic method [36] has been used to tune the PID gain. Simulation of the physical system has been performed by making use of the system transfer function G(s) and the following procedure:

1. Close the loop with only proportional term, i.e. setting K_I and K_D to zero.
2. Increase the proportional value from zero until it reaches the value K_u, in which the output has stable and consistent oscillation with period T_u. For this system: $K_u = 1.1,\ T_u = 0.025$ s.
3. Calculate the PID gains using Table 4.1(a). Results of different methods are summarized in Table 4.1(b).

Table 4.1 Ziegler-Nichols heuristic method (a) PID gain formulas depending on the controller used (b) results using Ku=1.1; Tu=0.025 s

Ziegler-Nichols method			
Control type	**Kp**	**Ti**	**Td**
PI	0.45 Ku	Tu/1.2	-
Classic PID	0.6 Ku	Tu/2	Tu/8
Pressen Integral rule	0.7 Ku	Tu/2.5	3Tu/20
PID no overshoot	0.2 Ku	Tu/2	Tu/3

(a)

Z-N method results					
Control type	**Ti**	**Td**	**Kp**	**Ki**	**Kd**
PI	0.0208	-	0.4950	23.7600	-
Classic PID	0.0125	0.0031	0.6600	52.8000	0.0021
Pressen Integral rule	0.0100	0.0038	0.7700	77.0000	0.0029
PID no overshoot	0.0125	0.0083	0.2200	17.6000	0.0018

(b)

The first objective of the project is the precision of the movement. The system must be capable of operating within nanometer intervals, minimizing the undesirable characteristics, such as overshoot or oscillation. Then initially, an overdamped system is wanted and the Ziegler-Nichols "PID no overshoot" gains are chosen for this study, as highlighted in Table 4.1 (b).

4.1.1 Root Locus Analysis

Root locus method is often used, during the analysis and synthesis phase of a controller, to study the behaviour of the poles of the closed loop transfer function when the PID gain varies. The three PID gains will be briefly explained and the impact on the closed loop control will be presented via root locus analysis in the following part of this section.

The first gain analysed is the proportional gain k_p. Its effect is proportional to the error between the required and the feedback signals (see Eq. 4.5). k_p increases the stiffness of the system and, consequently, its natural frequency. Merging Eqs. (3.7) and (4.5), it is clear in Eq. (4.6) how the proportional term acts firstly according to the actual position $x^*(t)$ (i.e. similarly to a feedforward term) and also dependently on the state of the system itself $x(t)$, which increases the stiffness of the system (i.e. the natural frequency). In this case study, the stiffness of the system is already big and the k_p parameter is smaller compared to this. So that, the final stiffness and the natural frequency will not dramatically change.

$$k_f k_d v_i(t) = k_p \left(x(t) - x^*(t) \right) \tag{4.5}$$

$$m_{tot} \ddot{x}(t) + c \dot{x}(t) + (k_t + k_p) x(t) = k_p \, x^*(t) \tag{4.6}$$

Employing uniquely the proportional term, the closed loop transfer function $L_P(s)$ in the Laplace domain results:

$$L_P(s) = \frac{15.21 K_P}{1.824 s^2 + 23.353 s + (129460 + 15.21 K_P)} \tag{4.7}$$

The root locus of the proportional closed loop control transfer function $L_P(s)$ is plotted on the diagram in Fig. 4.2. As expected, the roots of $L_P(s)$ move on two branches, which are straight lines parallel to the imaginary axis. The imaginary part of the eigenvalues of the system (i.e. ω) increases, while the real part (i.e. ω) remains constant. Thus, the stability index α/ω decreases.
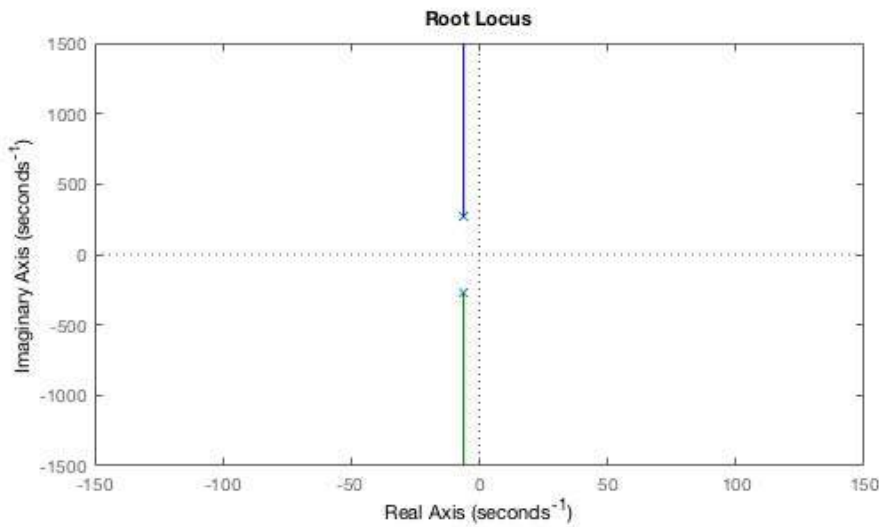
Figure 4.2 Root locus of the proportional control system $L_P(s)$

However, with only proportional feedback, the system is not capable of achieving the reference value under steady state conditions. Increasing the gain, the steady state error decreases, but it will be never eliminated.

Additionally, an high proportional term leads a growth of the instability and the over-shoot.

To eliminate the steady-state error, it is needed a controller in which the control action is proportional to both the error between the reference signal and the system response and to its integral in time. The integral term can be view as a lag action. In the complex plane shown in Fig. 4.3, for a harmonic signal, it is rotated by 90 clockwise with respect to the purely proportional action.
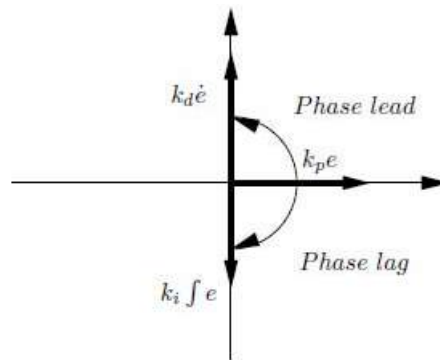

Figure 4.3 Proportional, Integrative and Derivative terms in the complex plane

The PI controller in the Laplace domain is represented by the following equation:

$$C_{PI}(s) = \frac{sK_P + K_I}{s} = K_P \frac{T_I s + 1}{T_I s} \qquad (4.8)$$

It can be noticed that, it presents a zero in -1/Ti and a pole in the origin. Then, the closed loop transfer function $L_{PI}(s)$ with PI controller becomes:

$$L_{PI}(s) = \frac{15.21(K_P s + K_I)}{1.824s^3 + 22.353s^2 + (129640 + 15.21K_P)s + 15.21K_I} \qquad (4.9)$$

The main effect of the integral action is to improve the behaviour under steady-state condition, by annulling it. The close loop transfer functions $L_P(s)$ and $L_{PI}(s)$ are compared on the diagram of Fig. 4.4. The integral control operates as a low-pass filter and attenuates the high frequency components making the control system less sensitive to disturbances. However, from the root locus in Fig. 4.4, it can be noted that if k_p increases, the stability of the system degrades until it became unstable when the two complex conjugate poles move on the real positive part of the complex plane.
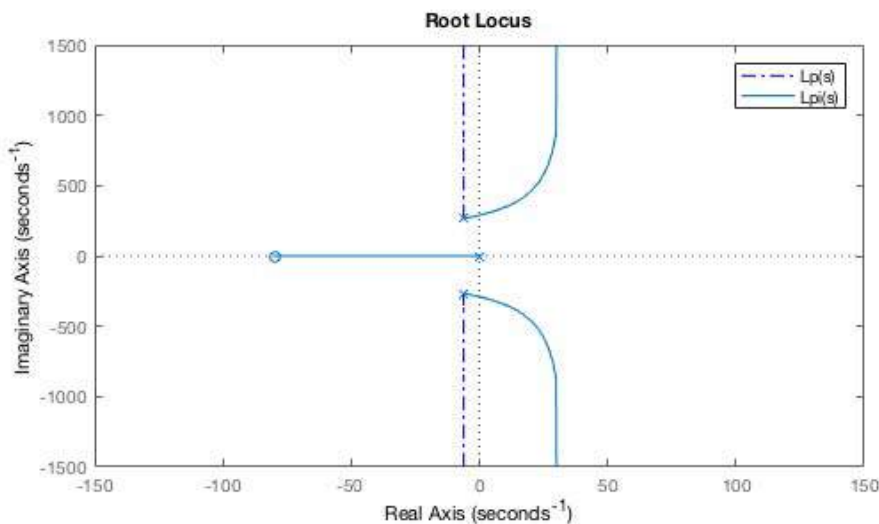
Figure 4.4 Root locus comparison between $\boldsymbol{L_P(s)}$ and $\boldsymbol{L_{PI}(s)}$

In order to avoid the problem of stability and oscillation, the derivative term is necessary. The derivative action is a term proportional to the error between the derivative of the required and the actual position. The derivative term acts as a high-pass filter, amplifying high frequency noise. In other terms, it produces an action which is proportional to speed. Into the complex plane of Fig. 4.3, it corresponds to indroduce a term which is rotated 90 degrees in an anti-clockwise direction respectively to the proportional term. The final closed loop transfer function has been calculated in Eq. (4.3). The close loop transfer functions $L_{PI}(s)$ and

$L_{PID}(s)$ are compared on the plot of Fig. 4.5. As can be noted, the transfer function $L_{PID}(s)$ presents:

- two complex conjugate poles $s_{1,2} = -6.134 \pm 266.346i$
- one pole at the origin
- one complex cojugate zero $s_{3,4} = -61.1 \pm 77.738i$

    It can be noticed in Fig. 4.5 that, the roots of the characteristic equation move onto branches of this locus, thus increase the system stability. Ideally, incresing the PID gains leads to achieve two poles with only negative real part. This corresponds to a damping factor equal to 1, so that a critically dumped system could be achieved. However, on the physical system, increasing too much the PID gain leads instability due to other unmodeled effects, such as vibrations. Eventually, on a step response analysis, the advantages of a derivative term are mainly a quick setting time and limited overshoot. As a result, it leads a good behaviour in term of transient response.
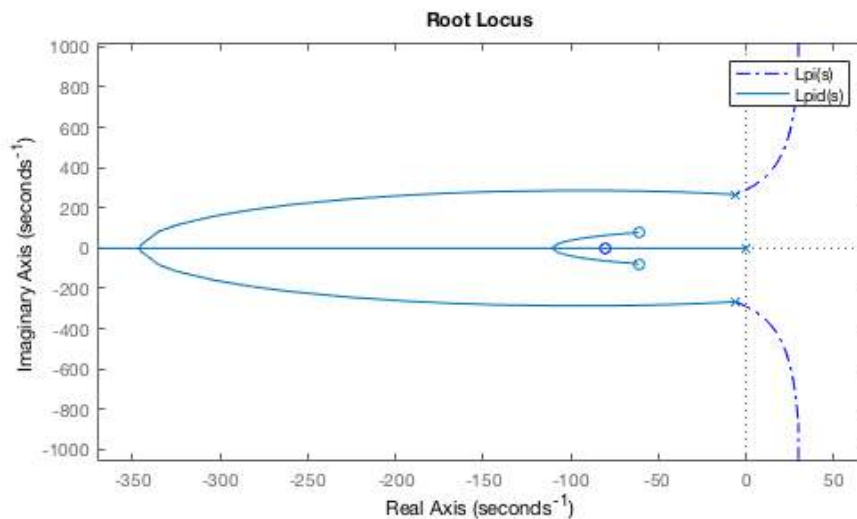
Figure 4.5 Root locus comparison between $L_{PI}(s)$ and $L_{PID}(s)$

59

4.1.2 Bandwidth estimate

Experiment for bandwidth estimation of the control system has been carried out. There are several experimental ways to estimate the bandwidth of a control system. The one that has been used makes use of a chirp signal generated in Matlab to detect how the system response to a chirp spectrum. After several experiments, the spectrum 1-10 Hz has been show in Fig. 4.6 with a total displacement range ± 0.1 mm.
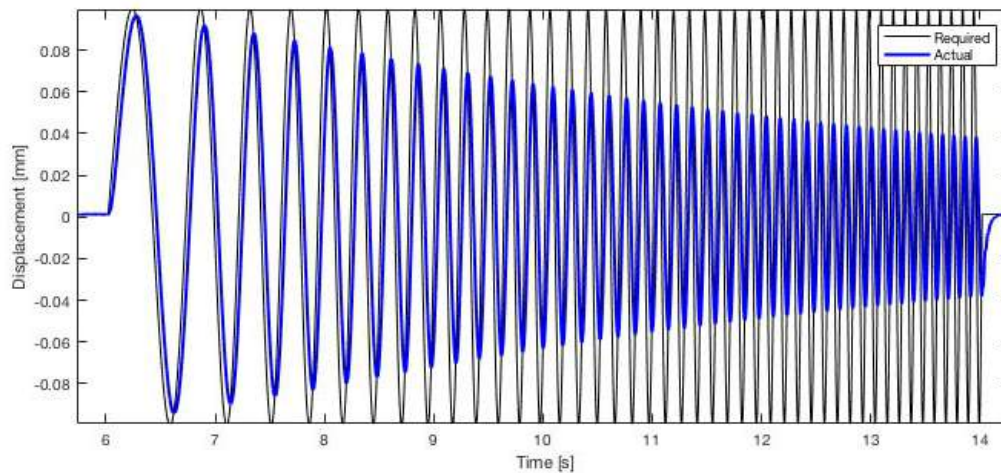

Figure 4.6 Response of the PID controller to a chirp signal with
frequency range 1-10 Hz and stroke 0.1 mm

It can be seen that the system follows within the 70% of the input value the required input displacement up to approximately 4 Hz. This means that the bandwidth of the system, considering the PID gains chosen, can be considered approximately 4 Hz analysing stroke equal to ± 0.1 mm.

In any case, the vibrational noise detected and studied in section 3.6 cannot be compensated with this controller since they have frequency equal to 40Hz.

4.2 Force Feedforward Control

The objective of this section is to present a force feedforward model which can control the system accurately without feedback signal. It could represent an accurate estimate of the system behavior which, if added on the PID model, enables a significant performance improvement [37].

A feedforward action should take into account of the system dynamics to calculate the required force needed to perform a certain displacement. In this case, a voice coil actuator (VCA) performs the actuation of the system. The principle of the VCA is to generate force $F(t)$ proportional to the current that flows through the motor coil $i_{act}(t)$ by the force sensitivity k_f, as explained in Section 3.3. Upstream on the system, the dSPACE board voltage signal $v_i(t)$ can be considered proportional to the current $i_{act}(t)$ by the gain k_d (explained in Eq. 3.3). On the other side, the force applied on the compliant mechanism can be also expressed using Newton's law. The dynamic of the compliant mechanism has been measured experimentally and it results to be a good representation of the system characteristics [23]. All these concepts are summarised in Eqs. (4.10) and (4.11).

$$F(t) = k_f i_{act}(t) = m_{tot}\ddot{x}(t) + c\dot{x}(t) + k_t x(t) \qquad (4.10)$$

$$i_{act}(t) = k_d V_i(t) \qquad (4.11)$$

where the constant values m_{tot}, c and k_t represent the dynamic properties of the compliant mechanism calculated in Section 2.4. The total mass m_{tot} corresponds to 1.824 kg, the damping factor c has been estimated equal to 0.023 and the experimental value of the overall stiffness k_t is 129460 N/m. The force sensitivity k_f and the driver gain k_d correspond to 35.14 N/A and 0.4329 A/V, respectively. Having obtained all the constant values of the dynamic equation, it is necessary to calculate the required displacement depending on the time with its corresponding velocity and acceleration, to obtain the required force F(t). To do that, different motion

laws can be employed, but the one which best suits a smooth displacement could be a quintic polynomial equation.

The Simulink model of the force feedforward open-loop scheme is illustrated in Fig. 4.7, where the "X[mm]", "Xd[mm/s]" and "Xdd[mm/s^2]" blocks represent the subsystems (which, when triggered by the "Single Input" block, read and reproduce data from the Matlab workspace) of the required displacement, velocity and acceleration, respectively. Once the model is triggered, the three signals corresponding to the three Newton's law components (see Eq. (4.10)) are generated simultaneously and added together to generate the required force F(t). The force signal has to be converted to a corresponding voltage signal: the conversion is done by the "N2V" gain block, which is equal to 0.065737 V/N. This has been calculated by combining Eqs. (4.10) and (4.11) through k_f and k_d.
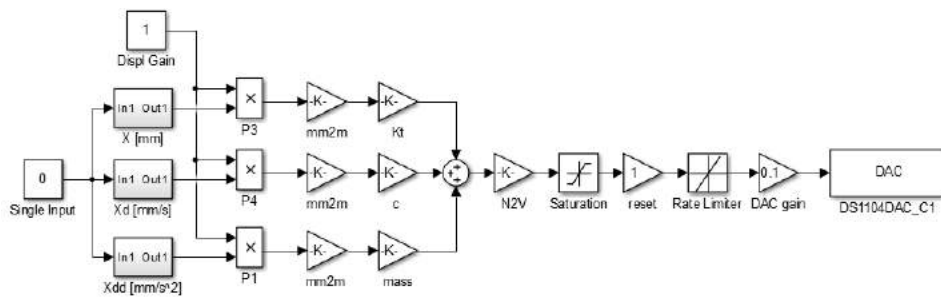
Figure 4.7 Force FeedForward control model

This model, compared to the PID controller, is expected to perform the required motion law with higher accuracy on the trajectory tracking (i.e. without delay). However, the feed forward action does not guarantee achievement of the desired position with nano positioning accuracy. In fact, if the required displacement is constant, once the transient is finished there will be always a steady-state error due to model inaccuracies. Conversely, the PID controller compensate precisely the steady-state error after the transient.

4.3 Force Feedforward and PID control

The PID controller described above generates a control action based on the error between the required and the feedback signals. For this reason, it results to respond with an intrinsic delay during the transient, which increases with the speed of the required input. Conversely, the feedforward action, which is estimated using the dynamic model and the desired motion law, is found to be more accurate during the transient, but it includes a steady state error due to the open-loop control disadvantages.

The combination of the two control models takes advantages of the fast response due to the feedforward terms and the high positioning accuracy due to the PID, which compensates the unmolded effects of the control model of the system. Indeed, the control scheme combining the PID and the force feedforward schemes has been implemented in Fig. 4.8 by merging the two Simulink models.
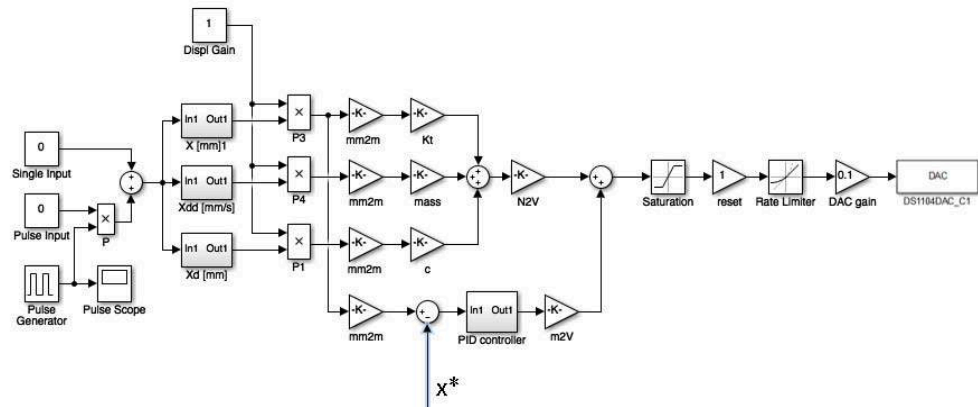
Figure 4.8 Force feedforward and PID control model

The two signals are added together after the conversion from newton to volts and from meter to volt on the force feedforward and the PID action respectively. A performance improvement is expected from this control model. Comparison of the control model results will be shown in the next chapter.

Chapter 5

Experimental Results

The results of the experimental tests carried out using the control schemes presented above are summarized in this chapter, in order to show the improvements achieved by combining the force feedforward action with the traditional feedback PID control. Due to the objectives of this project, quintic polynomial functions have been used as position trajectories. They assure adequate smoothness during the motion, and continuity the displacement, velocity and acceleration functions. The definition of a polynomial function is described in Eq. (5.1).

$$x(t) = a_0 + a_1 t + a_2 t^2 + \cdots + a_n t^n \tag{5.1}$$

Increase the grade n of the polynomial function makes it smoother and there are more boundary conditions to satisfy. A general definition of quintic polynomial motion law, with its derivative and double derivative, is given in Eqs. (5.2).

$$x(t) = a_0 + a_1 t + a_2 t^2 + a_3 t^3 + a_4 t^4 + a_5 t^5$$
$$\dot{x}(t) = a_1 + 2a_2 t + 3a_3 t^2 + 4a_4 t^3 + 5a_5 t^4 \tag{5.2}$$
$$\ddot{x}(t) = 2a_2 + 6a_3 t + 12a_4 t^2 + 20a_5 t^3$$

In order to solve that, it's necessary to know the initial and final conditions of position, velocity, acceleration and time. With these values we could impose the boundary conditions and find out the constants a_n depending on the time. The constants relative to the initial and final values are described in Eqs. (5.3).

$$a_o = x_i$$

$$a_1 = \dot{x}_i$$

$$a_2 = \frac{1}{2}\ddot{x}_i$$

$$a_3 = \frac{20(x_f - x_i) - (8\dot{x}_f + 12\dot{x}_i)(t_f - t_i) - (3\ddot{x}_f - \ddot{x}_i)(t_f - t_i)^2}{2(t_f - t_i)^3} \quad (5.3)$$

$$a_4 = \frac{30(x_i - x_f) + (14\dot{x}_f + 16\dot{x}_i)(t_f - t_i) + (3\ddot{x}_f - 2\ddot{x}_i)(t_f - t_i)^2}{2(t_f - t_i)^4}$$

$$a_5 = \frac{12(x_f - x_i) - 6(\dot{x}_f + \dot{x}_i)(t_f - t_i) - (\ddot{x}_f - \ddot{x}_i)(t_f - t_i)^2}{2(t_f - t_i)^5}$$

All the equations describing position, velocity and acceleration of the motion laws studied as well as their corresponding data vectors have been calculated and saved in Matlab format for a subsequent use in the Simulink model. The sample time used to generate the equation vectors is 0.002 s.

Some examples of the motion laws studied are shown and compared below in Fig. 5.1 and in Fig 5.2. Displacement, velocity and acceleration are plotted. The two functions plotted in Fig. 5.1 have been generated with two different traverse time (i.e. 0.5 and 2 s), but with the same displacement (i.e. 0.1 mm). The stroke can be modified afterwards automatically using a gain in the Simulink model. An example is given in Fig 5.2 in which there are three functions with the same traverse time (i.e. 0.5 s) and different displacement.
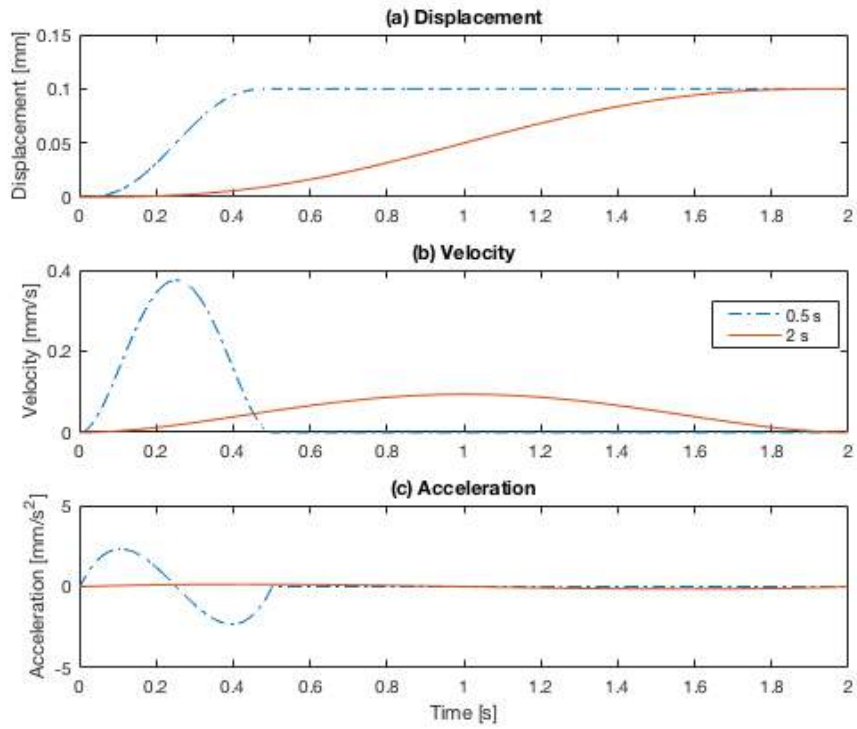
Figure 5.1 Motion law comparison with displacement 0.1 mm and
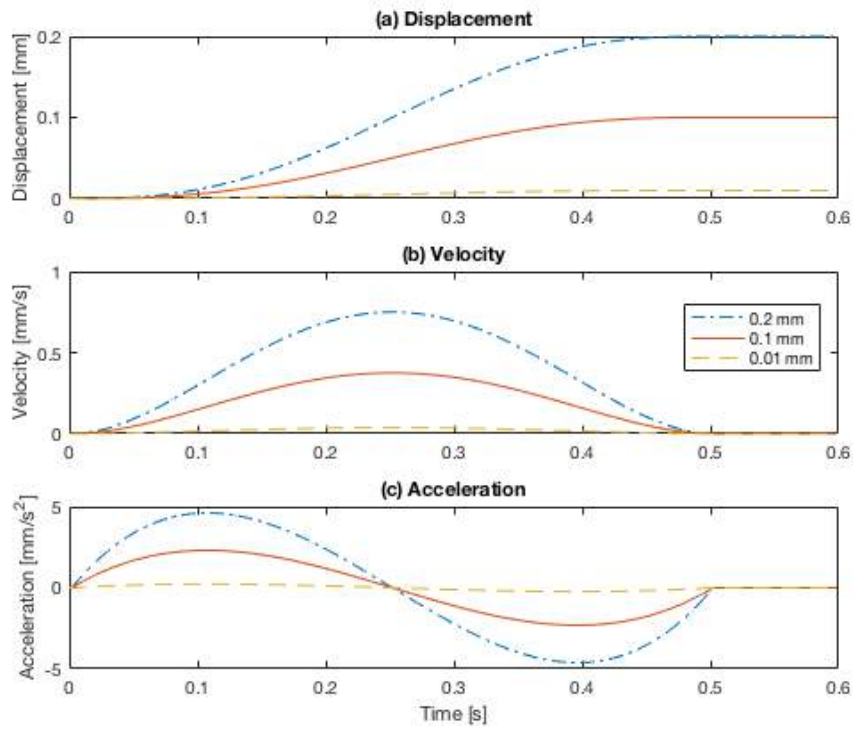different traverse time

Figure 5.2 Motion law comparison with traverse time 0.5 s and
different displacement

Different traverse time and displacement will be tested and compared in all the range studied of the nano-positioning system with a trajectory tracking and performance analysis which include both positioning and path studies. The positioning analysis, which does not take into account of the transient phase, will result similar with the two controller synthesized. Conversely, the path analysis will show off the ability of the force feedforward controller to follow the required position getting rid of the intrinsic delay of the PID controller.

5.1   Trajectory Tracking Analysis

Trajectory tracking analysis has been done and the results are summarised in this section to show the behavior of the controller over two distinct displacement ranges (i.e. 0.2 mm and 100 nm) in both the positive and negative regions, in order to prove the ability of the controllers in the full linear range (± 0.2 mm). Eight different trajectories are shown in Fig. 5.3 and Fig. 5.4: the first 4 functions shown in Fig. 5.3 have a traverse time 2 s with motion ranges as specified above, the second 4 functions shown in Fig. 5.4 have a traverse time 0.5 s over the same motion ranges.
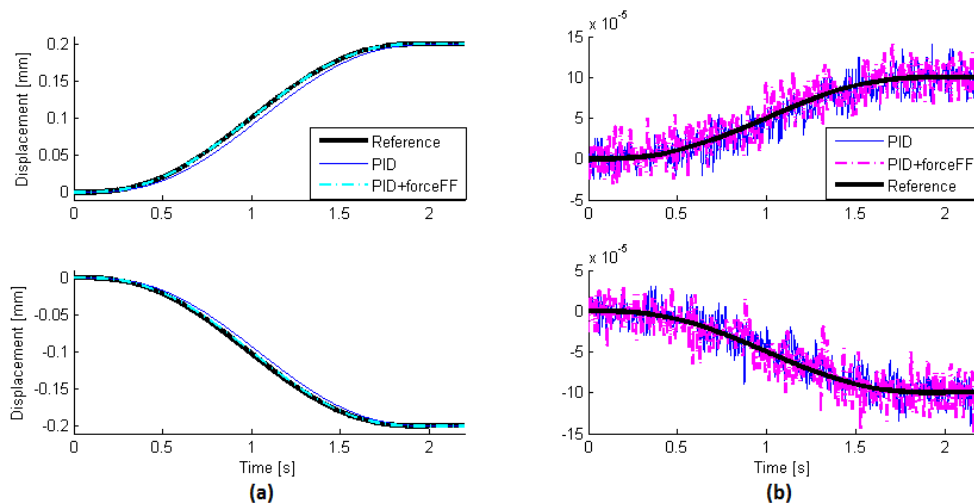

Figure 5.3 Results comparison with a 2 s traverse time
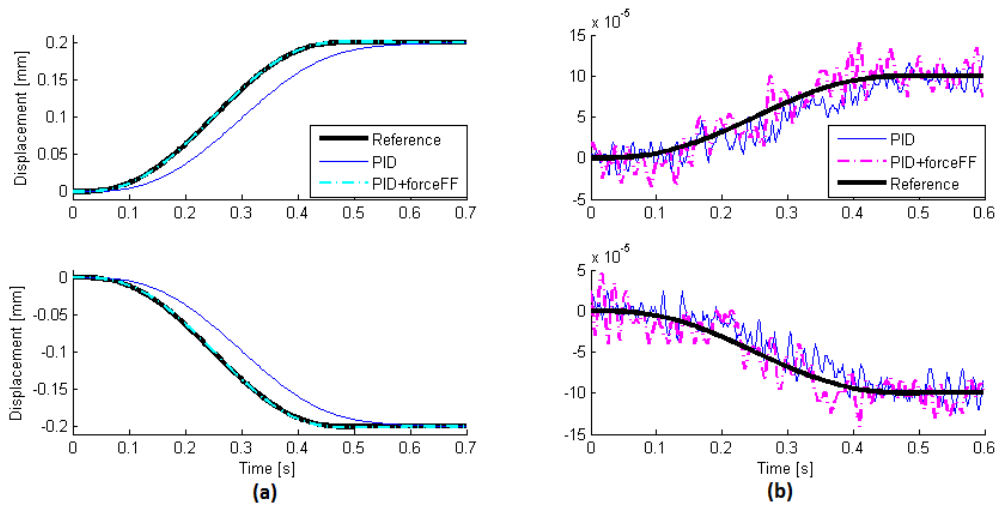
(a) ± 0.2 mm (b) ± 100 nm

Figure 5.4 Results comparison with a 0.5 s traverse time

(a) ± 0.2 mm (b) ± 100 nm

The results show the improvements on the control effectiveness using the PID controller combined with the force FF terms. In particular, it is evident in the Fig. 5.4 (a) that the tracking error decreases significantly in the presence of a swift trajectory, and that an accurate tracking of a desired reference is assured. Figures 5.3 (b) and 5.4 (b), which show ± 100 nm displacements, indicate vibrational disturbances with a range of about ± 30 nm on the system. These disturbances decrease from a range of ± 100 nm to approximately ± 30 nm using the selected anti-vibrational mounts described in section 3.6. Despite these disturbances, the system is able to follow the requested trajectory. These vibrations will be considered on the repeatability performances, in which the distribution of the positions has been studied using standard deviation.

Finally, additional comparisons have been carried out to analyse the velocity and the acceleration error. Velocity and acceleration comparisons of the motion law in Fig 5.4 (a) (displacement 0.2 mm, traverse time 0.5 s) have been plotted in Figures 5.5 (a) and 5.5 (b), respectively. It is evident that the PID controller combined with the force FF signal achieved the best results.
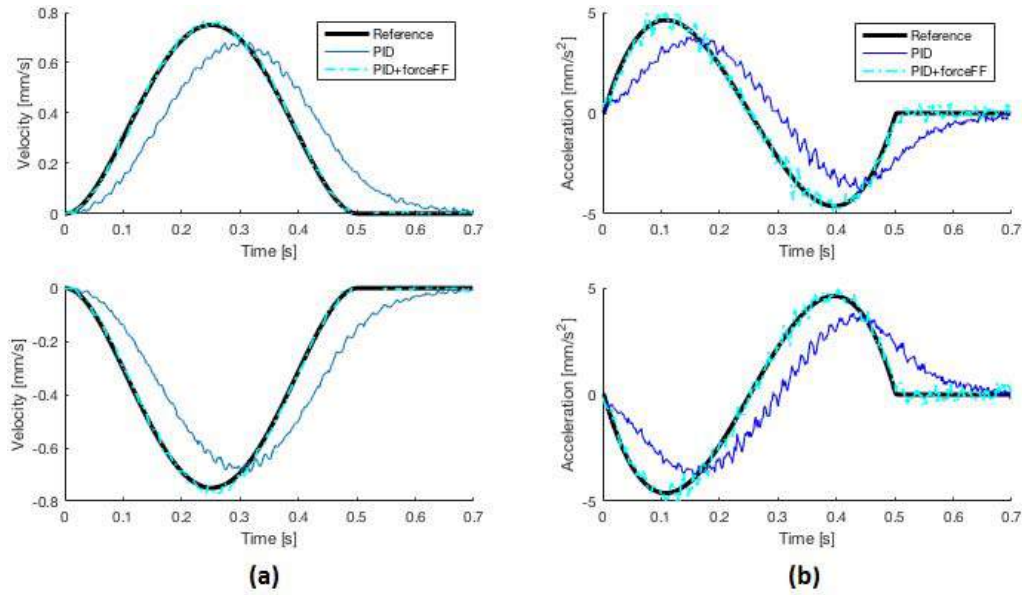
69

Figure 5.5 Displacement 0.2 mm, traverse time 0.5 s

(a) Velocity (b) Acceleration

5.2   Performance analysis

This section presents the extended experimental results performed with the nano-positioning system using the control schemes discussed in Section 2 in terms of resolution, accuracy and repeatability. These (see Fig. 5.6) are commonly used to define capability of manipulators. In general, there are many procedures that describe how to calculate manipulator performances [38]–[40], but there is no standard test used to come up with these values because they depend on several variables. However, this analysis is facilitated since some variables do not have to be considered. This project involves the study of one axis of a 3 DOF nano-positioning system for the reasons explained in [23]. Additionally, the payload for the hypothetical applications is often negligible compared with the mass of the system. The standard which has been considered for the definitions and analysis of accuracy and repeatability is ISO 9283 [41].
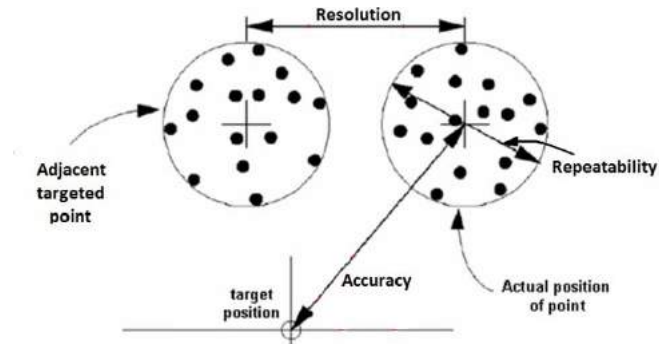
Figure 5.6 Resolution, accuracy and repeatability
representation

5.3.1 Resolution (RE)

Control resolution is defined as the smallest incremental change that the control system can distinguish. [38]. Essentially, it is the smallest move that the manipulator can make. Fig. 5.6 shows two spaced points representing where the system may be commanded to go. The distance between them is the control resolution. The linear encoder has a resolution of 5 nm, but, due to the vibrational disturbance also shown in Fig. 5.3 (b) and Fig. 5.4 (b), the minimum step that can be recognised defines the resolution $RE = 30$ nm (see Fig. 5.7).

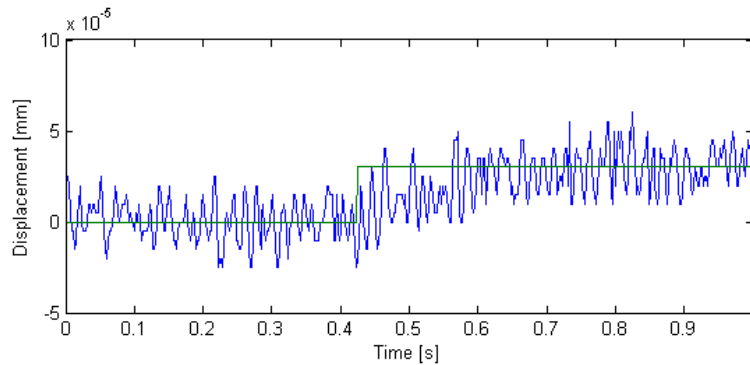**Figure 5.7** Resolution test: 30 nm step

5.3.2 Positioning Accuracy (AP) and Repeatability (RP)

Accuracy is the ability of the nano-positioning system to approach an arbitrary point within its workspace. Position accuracy is the difference between the required position and the mean of the reached positions

when approaching the same required position from the same direction (see Eqs. (5.4)).

$$AP = x_c - \bar{x} \qquad with \qquad \bar{x} = \frac{1}{n}\sum_{j=1}^{n} x_j \qquad (5.4)$$

where x_c is the required position, x_j represents the j-th reached position, $\bar{x}$ is the mean of all the reached positions and n is the total number of measurements.

Experimental measurements have been carried out to analyse the full linear range of ±0.2 mm. Twelve displacements have been measured: ±0.2 mm, ±0.1 mm, ±0.05 mm, ±0.01 mm. ±0.001 mm and ±0.0001 mm. Each displacement analysed has been repeated thirty times as requested in [41]. Finally, 12 values of AP have been calculated and plotted in Fig. 5.8. The results indicate a position accuracy on the linear region studied equal to AP=5 nm.
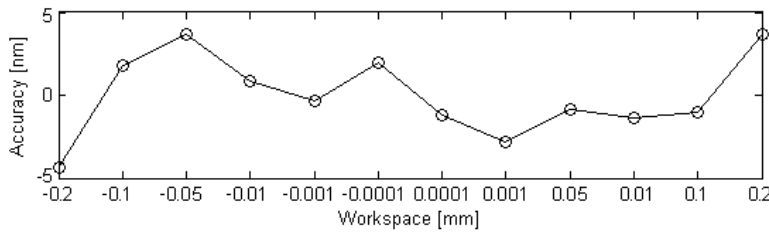

Figure 5.8 Position accuracy along the linear range ±0.2 mm

Repeatability is defined as the ability of the manipulator to reposition itself at the same point of the workspace. It expresses the closeness of agreement between the reached positions x_j after n cycles using the same required position x_c in the same direction. For a given x_c the repeatability is defined as follows:

$$RP = \bar{l} + 3\sigma_l \qquad with \qquad \bar{l} = \frac{1}{n}\sum_{j=1}^{n} l_j \qquad l_j = x_j - \bar{x} \qquad (5.5)$$

where l_j is the distance between the j-th reached position and the barycentre of the reached position $\bar{x}$ (Eq. (5.5)), n is the number of cycles required and is given equal to 30, $\bar{l}$ is the mean of the distances l_j. The standard deviation σ_l of the positions reached is expressed in Eq. (5.6). Three times of σ_l is considered in the value of RP to take into account of 99.74% of the data.

$$\sigma_l = \sqrt{\frac{\sum_{j=1}^{n}\left(l_j - \bar{l}\right)^2}{n-1}} \tag{5.6}$$

Similarly to the accuracy analysis, the whole workspace considered has been tested using the same 12 displacement values. The results are summarised in Fig. 5.9 in which is plotted the values of the mean distance $\bar{l}$, RP considering one σ_l (see RP (1σ)), which includes 68.27% of the values encountered and RP considering three σ_l (see $RP(3\sigma)$) as described in Eq. (10) which includes 99.73% of the values encountered.
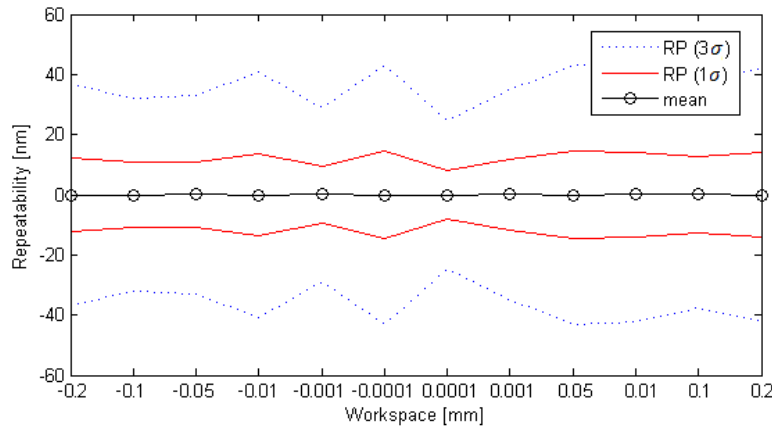

Figure 5.9 Position repeatability along the linear range ± 0.2 mm

The results show the value of RP, as described in Eq. (5.5), as being approximately equal to $RP = 35$ nm. The $\bar{l}$ values are approximately null, which demonstrate that the system approaches the required points

correctly in the full range studied. Despite this, the repeatability results differ significantly from the $\bar{l}$ values because the vibrational disturbances cause fluctuation of the system around the targeted point.

5.3.3 Path Accuracy (AT) and Repeatability (RT)

Path accuracy and path repeatability are studied to analyse the precision of the manipulator to follow paths. Their definitions are independent of the shape of the required path. Path accuracy characterizes the ability of a manipulator to move its interface along the required path in the same direction n times. AT is the maximum path deviation between the positions of the required path and the barycentre line of the cluster of the positions along the path reached (see Eq. 5.7). The standard ISO includes also indications regarding the difference between orientations, but it is not necessary in this study.

$$AT = \max (\bar{x}_i - x_{ci}) \qquad with \qquad \bar{x}_i = \frac{1}{n} \sum_{j=1}^{n} x_{ij} \qquad (5.7)$$

Where j represents the number j-th cycle, i represents the i-th point of the analysed path, x_{ci} is the coordinate of the i-th point on the required path, x_{ij} is the coordinate of the i-th point of the j-th reached path, $\bar{x}_i$ represents the coordinate of the i-th point of the barycentre line of the cluster of the positions along the path reached. The number of cycles required n on the path analysis is given equal to 10 [41].

The path accuracy analysis has been carried out using measurements which cover the full linear range studied (i.e. ± 0.2 mm). Twelve displacements have been measured: ± 0.2 mm, ± 0.1 mm, ± 0.05 mm, ± 0.01 mm, ± 0.001 mm and ± 0.0001 mm. Each displacement has been tested using both the PID and the PID+Feedforward controllers.

As an example, a full path accuracy plot is provided to show the overall error trend during the traverse time. The path considered is a 0.1

mm displacement with 0.5 s traverse time. Fig. 5.10 shows the required path in the above part and below the path accuracy values obtained using both the PID and the PID + Force FF control schemes.
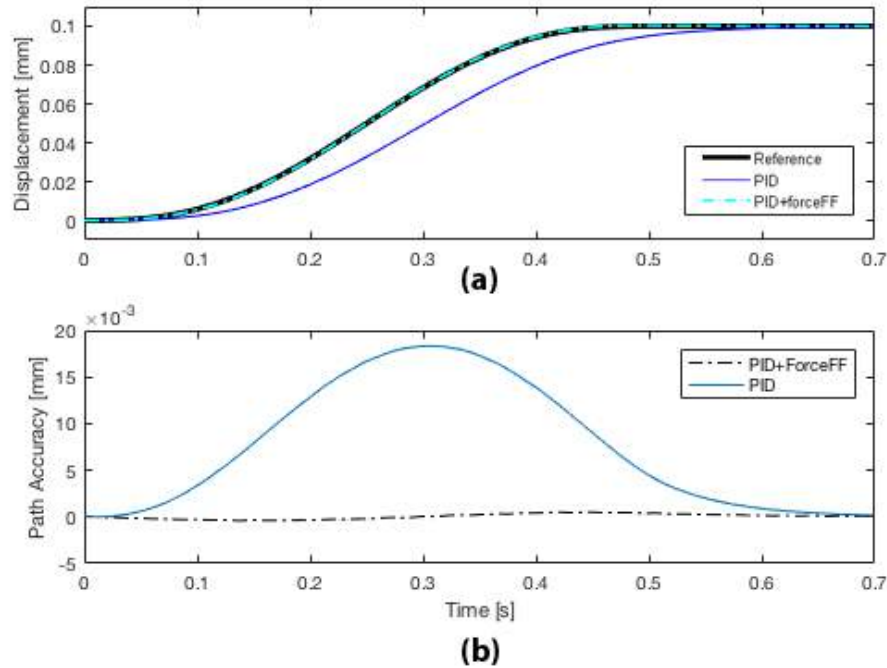

Figure 5.10 Full path accuracy: 0.1 mm displacement 0.5 s traverse time

(a) trajectory tracking result (b) full path accuracy

It can be seen that the PID + Force FF control achieves a value of path accuracy much smaller than the PID control. The AT value (i.e. the maximum differences between the barycentre line of the reached path and the required path) is measured when the velocity reaches its peak. The AT values have been extracted for each of those displacements studied and plotted in Fig. 5.11. It can be seen that, in both of the control strategies, increasing the velocity of the movement leads an increase of the AT value. However, while the maximum AT value reached using the PID control is approximately 0.038 mm, the PID+Force FF control shows an AT value of approximately 280nm in its worst case.
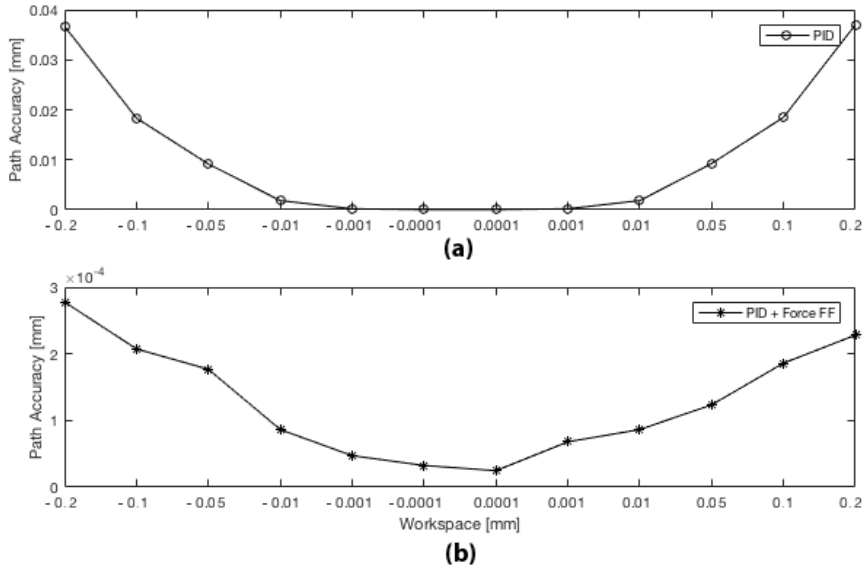
Figure 5.11 Path accuracy along the overall range ±0.2 mm

(a) PID control results (b) PID+Force FF results

Similarly, the path repeatability (RT) represents the closeness of the agreement between the reached paths for the same given path followed n cycles in the same direction. It is the maximum repeatability deviation RT_i, corresponding to the i-th point along the path. RT and the correlated quantities are explained in Eqs. (5.8) and (5.9).

$$RT = max \; RT_i = \max(\bar{l}_i + 3\sigma_{li}) \tag{5.8}$$

$$\bar{l}_i = \frac{1}{n}\sum_{j=1}^{n} l_{ij} \qquad l_{ij} = x_{ij} - \bar{x}_i \qquad \sigma_{li} = \sqrt{\frac{\sum_{j=1}^{n}\left(l_{ij} - \bar{l}_i\right)^2}{n - 1}} \tag{5.9}$$

where $\bar{x}_i$ and x_{ij} are as defined above for AT, l_{ij} is the difference between the reached position (of the i-th point of the path during the j-th cycle) and the barycenter of the reached positions, $\bar{l}_i$ is the mean of the distances l_{ij} obtained on the i-th point of the path, σ_{li} is the standard deviation of the position reached on the i-th point of the path. Three standard deviations are considered in the value of RT to take into account of 99.74% of the data. As an example, a full path repeatability plot is provided to show the overall trend during the traverse time. The same

76

path used for the path accuracy analysis has been considered: 0.1 mm displacement with 0.5 s traverse time. Fig. 5.12 shows the required path in the above part and below the path repeatability values obtained using both the PID and the PID + Force FF control schemes.
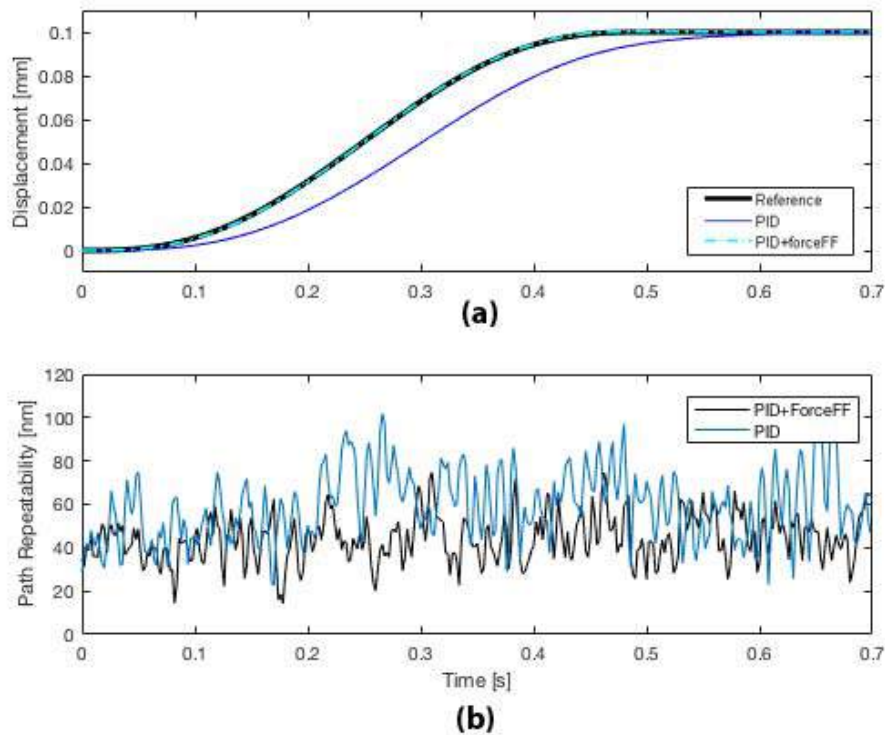

Figure 5.12 Full path repeatability: 0.1 mm displacement 0.5 s traverse time
(a) trajectory tracking result (b) full path repeatability

The results exploit that the repeatability of the two control schemes used have achieved good RT values. However, a slight improvement has been recorded using the PID+Force FF control. The same displacements used for the path accuracy analysis have been used to test the RT within the overall range analysed ± 0.2 mm. The RT values have been extracted for each of those displacements and plotted in Fig. 5.13. It has been confirmed that the PID control has recorded slightly higher values of the RT, but they both achieved good results. The PID+Force FF control recorded a RT worst-case value approximately 75% lower compared to the one recorder with PID control. Finally, it can be observed that the RT values are approximately consistent in both the control strategies used.

This means that the repeatability is not affected by the velocity rate, but it is dependent on the vibrational disturbances which affect the nano-positioning system consistently.
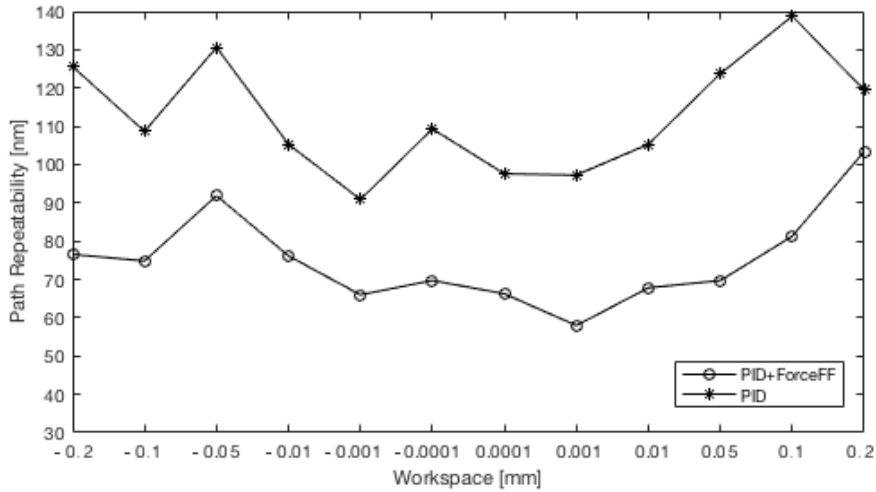

Figure 5.13 Path repeatability results of the two control schemes studied along the overall range analysed ±0.2 mm

5.3   Friction Deadband

A deadband on the physical system has been detected during the early stage experimental measurements. Firstly, using a PID controller an unjustified delay has been found to affect the beginning of each movement when changes of direction occurred. An example is provided in Fig. 5.14, in which a 0.1 mm displacement with 2 s traverse time motion law has been plotted in both the directions. It can be observed that the PID controller had to reach a certain amount of error before making the manipulator moving. This amount of error corresponds to an equivalent force which is needed to make the system moving. Therefore, this delay could correspond to a friction problem which make the system slow to react to change of direction.
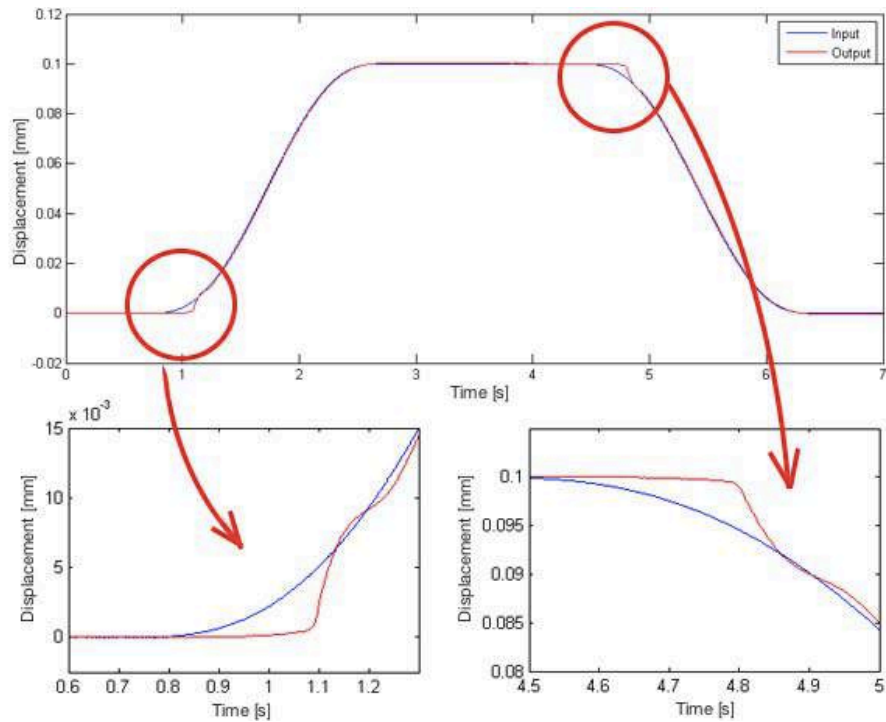
Figure 5.14 Deadband observed using PID control:
0.1 mm displacement, 2 s traverse time

Secondly, the force feedforward open-loop control has been tested using different types of motion laws with the aim to investigate if the problem could be related either to a friction on the system or to a incorrect system model. A result of the tests carried out is plotted in Fig. 5.15.
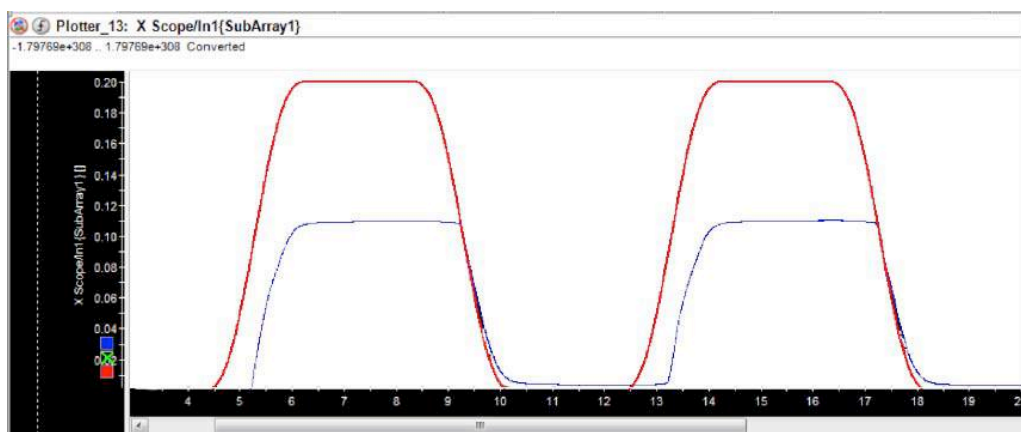

Figure 5.15 Dead band observed using Force FF open-loop control

It can be observed that the actual displacement (i.e. blue line on the graph) reached approximately 50% of the required displacement (i.e. red line on the graph). Additionally, the delay at the beginning at each change of direction is recorded also in this case. Subsequently, static analysis of the feedforward model has been conducted in order to figure out the problem explained above. The input signal used was small steps to detect the exact amount of displacement, and calculate the corresponding force, that was necessary to make the manipulator moving. This could represent the deadband on the system. A result is plotted in Fig. 5.16.
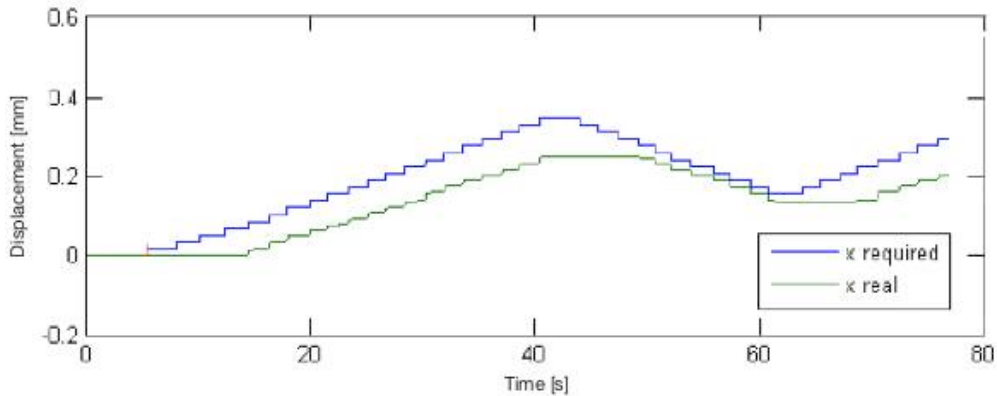

Figure 5.16 Deadband observed using step analysis

The result shows that at the 5th step (i.e. 0.1 mm, corresponding to approximately 13 N) there was a response of the system. Before this point the system was not responding, after this point the system responded with steps approximately proportional to the required signal maintaining the delay accumulated at the beginning. Additionally, when the system was commanded to come back, it responded after the same interval. The critical step (i.e. 0.1 mm, corresponding to approximately 13 N), found to make the system responds with such a delay, corresponded to the deadband of the system. This dead band could be associated to the force necessary to overcome the friction on the physical system.

Experimental identification of the system deadband has been carried out to have a better understanding of the problem and a starting point from which compensation could be done. A method that extracts the

friction characteristic from the loop error of a state feedback motion controller is presented in [42]. The controller is designed by incorporating all the available system knowledge into the model. The unmodeled dynamics of the system (i.e. friction) will appear as a state error on the controller (see Fig. 5.17). Plotting the value of the feedback force versus the position, the friction deadband loop can be identified (see Fig. 5.18).
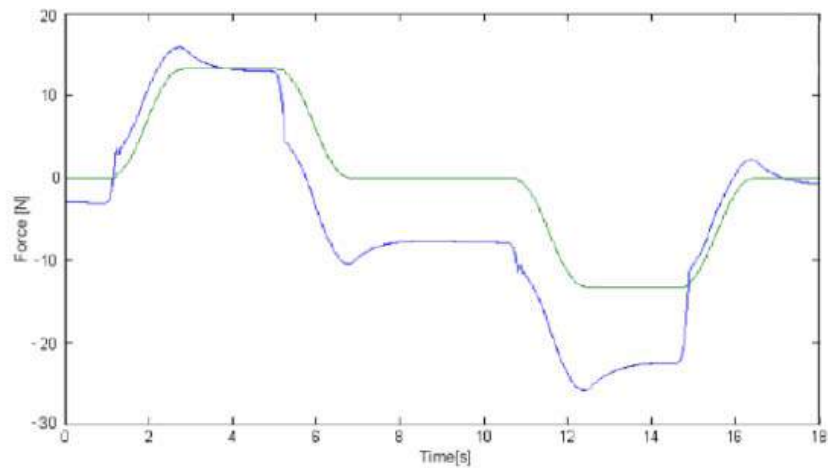

Figure 5.17 Friction identification: comparison between force required and force feedback as a state error
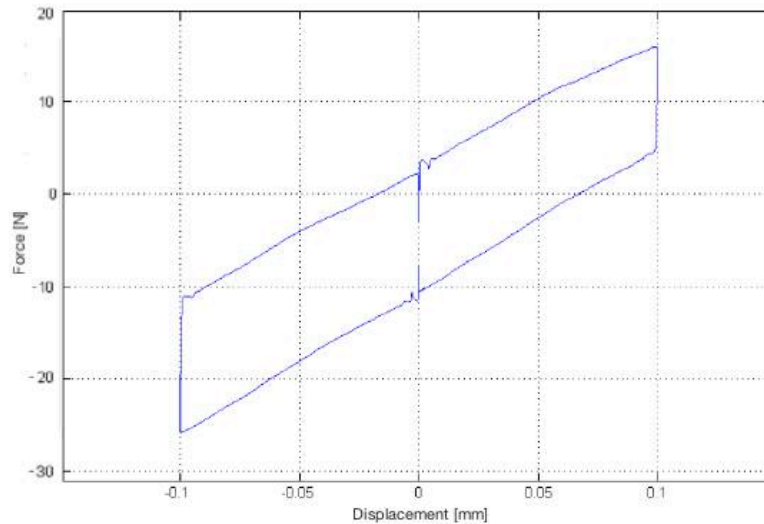

Figure 5.18 Friction identification: Force feedback VS Position

81

This model could be used to implement nonlinear friction compensation in a feedforward format. By applying this method in an iterative scheme, the performance of the system can be continually improved. Therefore, a feedforward term containing the gap of force equivalent to overcome the friction has been added on the force feedforward control scheme. The results, adding an extra feedforward term to compensate the friction deadband, are plotted in Fig. 5.19.
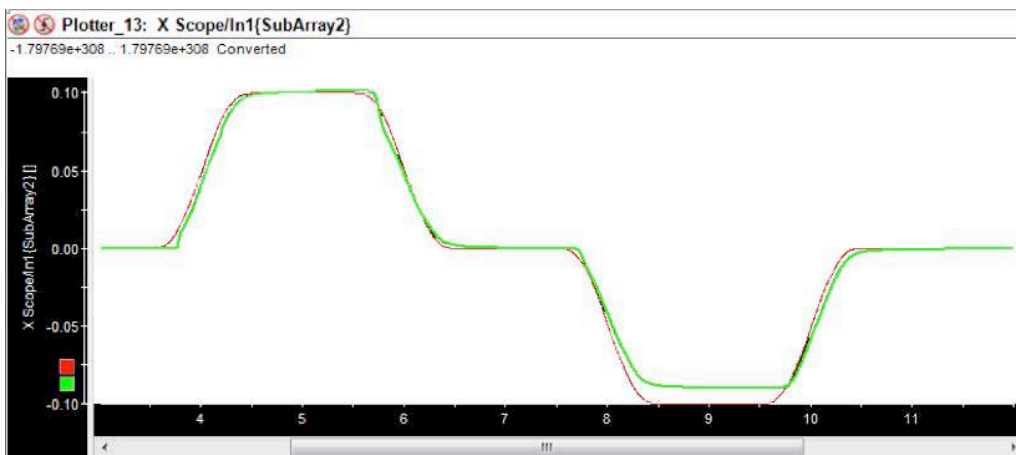

Figure 5.19 Friction compensation with an extra feedforward term: required position (red line), actual position (green line)
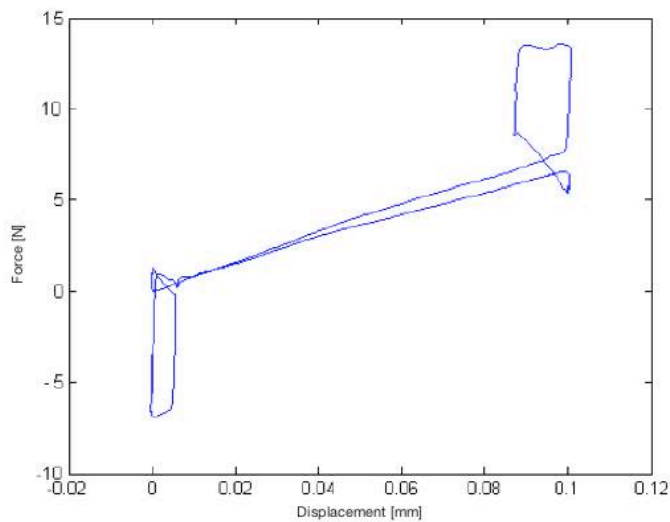

Figure 5.20 Friction compensation: Force feedback VS Position

As it can be seen, the friction effect has been dramatically reduced. However, the final result is not satisfactory enough because there are still problems at the beginning and at the end of the movement (see Fig. 5.20). Additionally, it can be noticed in Fig 5.19 that on the negative part of movement the system does not reach the required position.

After several experiments on the system in order to analyse the friction deadband, in which every component (driver, actuator, compliant device and encoder) has been analysed and tested, it has been figured out that the actuator was the cause of such behavior. The problem was an assembly issue of the actuator. It has to respect some clearances between the coil and the magnet. Particularly, as specifiend in the actuator datasheet [30], the linear actuator parameters section says that the clearances on each side of the coil should be 0.51 mm. In the physical system, the assembly of the actuator did not respect this requirement. Therefore, some contacts between the two parts of the actuator led the friction deadband detected above. After fixing this assembly issue building a new frame for the actuator, the nano-positioning system shown its ability to follow properly the required position. All the results shown in the trajectory tracking and in the performance anlysis have ben carried out after this adjustment.

Chapter 6

Conclusion

A mechatronic system designed for accurate nano-positioning has been described modeled and controlled in this thesis. The analysis has been restricted to one of the three orthogonal translational axes of the device being the dynamics of such axes independent. Some relevant characteristics of the compliant mechanism involved (i.e. stiffness and viscous damping) have been investigated theoretically and experimentally. Anti-vibrational mounts have been selected and installed on the aluminum frame to reduce vibrational disturbances. A reduction of the vibration from $\pm 100\,nm$ to $\pm 30\,nm$ has been demonstrated. The transfer function of a single axis of the system has been computed. This mechatronic system is designed to meet the very accurate precision requirements of both biomedical injection and fast tool servo manufacturing applications. The control design has been discussed and the control schemes used have been described. Force feedforward terms have been calculated using Newton's law with the system characteristic values calculated. It has been demonstrated that the force feedforward terms are well estimated. They have been tested using an open-loop control and they have shown a micrometric control quality. When added to the PID, the feedforward terms improve the controller performances in terms of path tracking capability and in particular they considerably improve the system response. Through a performance analysis based on

the standard ISO 9283, the mechatronic system has been proved to have a control resolution of 30 nm, additionally a position accuracy of approximately 5 nm and a position repeatability of 35 nm were achieved considering three standard deviations. Path performance analysis has been carried out comparing both the control schemes results. The path accuracy value using the PID control is approximately 0.038 mm. Conversely, the PID+Force FF control shows a path accuracy of approximately 280nm in its worst case. The path repeatability recorded using the PID control corresponds to 140 nm, while the PID+Force FF control showed a slight improvement with a value of 90 nm. Finally, during the early stage experiments, a dead band on the system has been identified, compensated and finally eliminated to obtain best performances.

The possible future work, which could improve the overall performance of the nano-positioning system, involves:

- To change the driver of the system, which is the major cause of vibration disturbances on the actual physical system. Changing the actuation, the bandwidth of the system can increase and consequently compensate vibration.
- To extend the range of motion of the device from ±0.2 mm to ±1 mm, further increasing in this way its applicability. This improvement requires a non-linear control scheme, which can compensate the detected non-linearity of the compliant mechanism.
- To extend the controlled degree of freedom from one to three.

References

[1] "All On Robots - robotics history, types of robots, industrial, toys and more." [Online]. Available: http://www.allonrobots.com/. [Accessed: 27-Aug-2017].

[2] H. Li, "Approaches to the synthesis, modelling and optimisation of spatial translational compliant parallel mechanisms," *PhD Thesis - UCC Cork*, 2016.

[3] S. Bashash and N. Jalili, "Robust Adaptive Control of Coupled Parallel Piezo-Flexural Nanopositioning Stages," *IEEE/ASME*, vol. 14, pp. 11–20, 2009.

[4] M. I. Frecker, K. M. Powell, and R. Haluck, "Design of a Multifunctional Compliant Instrument for Minimally Invasive Surgery," *J. Biomech. Eng.*, vol. 127, no. 6, pp. 990–993, Jul. 2005.

[5] H. Li, R. Ibrahim, and K. Cheng, "Design and principles of an innovative compliant fast tool servo for precision engineering," *Mech. Sci.*, vol. 2, no. 2, pp. 139–146, Jul. 2011.

[6] L. L. Howell, *Compliant Mechanisms*. John Wiley & Sons, 2001.

[7] H. Li, G. Hao, and R. C. Kavanagh, "A New XYZ Compliant Parallel Mechanism for Micro-/Nano-Manipulation: Design and Analysis," *Micromachines*, vol. 7, no. 2, p. 23, Feb. 2016.

[8] J. J. Gorman and N. G. Dagalakis, "Force Control of Linear Motor Stages for Microassembly," pp. 615–623, Jan. 2003.

[9] E. Sung, J. Slocum Alexander H., R. Ma, J. F. Bean, and M. L. Culpepper, "Design of an Ankle Rehabilitation Device Using Compliant Mechanisms," *J. Med. Devices*, vol. 5, no. 1, Jan. 2011.

[10] S. Kota, J. Joo, Z. Li, S. M. Rodgers, and J. Sniegowski, "Design of Compliant Mechanisms: Applications to MEMS," *Analog Integr. Circuits Signal Process.*, vol. 29, no. 1–2, pp. 7–15, Oct. 2001.

[11] G. Hao and R. B. Hand, "Design and static testing of a compact distributed-compliance gripper based on flexure motion," *Arch. Civ. Mech. Eng.*, vol. 16, no. 4, pp. 708–716, Sep. 2016.

[12] "A Method for the Design of Compliant Mechanisms With Small-Length Flexural Pivots | Journal of Mechanical Design | ASME DC." .

[13] S. Awtar, "Synthesis and analysis of parallel Kinematic XY flexure mechanisms," Thesis, Massachusetts Institute of Technology, 2003.

[14]   G. Hao, H. Li, X. He, and X. Kong, "Conceptual design of compliant translational joints for high-precision applications," *Front. Mech. Eng.*, vol. 9, no. 4, pp. 331–343, Dec. 2014.

[15]   S. Awtar and A. H. Slocum, "Constraint-Based Design of Parallel Kinematic XY Flexure Mechanisms," *J. Mech. Des.*, vol. 129, no. 8, pp. 816–830, May 2006.

[16]   H.-J. Su, D. V. Dorozhkin, and J. M. Vance, "A Screw Theory Approach for the Conceptual Design of Flexible Joints for Compliant Mechanisms," *J. Mech. Robot.*, vol. 1, no. 4, pp. 041009-041009-8, Sep. 2009.

[17]   J. B. Hopkins and M. L. Culpepper, "Synthesis of multi-degree of freedom, parallel flexure system concepts via Freedom and Constraint Topology (FACT) – Part I: Principles," *Precis. Eng.*, vol. 34, no. 2, pp. 259–270, Apr. 2010.

[18]   S. Awtar, "Analysis and synthesis of planer kinematic XY mechanisms," Sc. D. thesis, Massachusetts Institute of Technology, Cambridge, MA, 2004.

[19]   J. P. Merlet, *Parallel Robots*. Springer Science & Business Media, 2006.

[20]   "COMPARISON OF THE CHARACTERISTICS BETWEEN SERIAL AND PARALLEL ROBOTS - ProQuest." [Online]. Available: https://search.proquest.com/openview/68e7b203685a1c67d53651e 76d551244/1?pq-origsite=gscholar&cbl=616471.

[21]   Y Tian, B Shirinzadeh, D Zhang, Y Zhong, "Modelling and analysis of a three-revolute parallel micro-positioning mechanism," *Proceedings of the Institution of Mechanical Engineers, Part C: Journal of Mechanical Engineering Science.* .

[22]   G. Hao and X. Kong, "A Novel Large-Range XY Compliant Parallel Manipulator With Enhanced Out-of-Plane Stiffness," *J. Mech. Des.*, vol. 134, no. 6, pp. 061009-061009-9, May 2012.

[23]   R. Sandon, H. Li, F. F. Ferro, A. Trevisani, R. Kavanagh, G. Hao, "High-Performance Control of a Single-Axis Compliant Nano-Positioning System: Design." (Submitted to IMC34 in Sligo, Ireland), Jun-2017.

[24]   G. Hao, H. Li, and G. Joseph, "Extended Nonlinear Analysis of Exactly-Constrained Compliant Compound Parallelogram Mechanisms," p. V05AT08A001, Aug. 2015.

[25]   G. Hao and H. Li, "Nonlinear Analytical Modeling and Characteristic Analysis of a Class of Compound Multibeam Parallelogram Mechanisms," *J. Mech. Robot.*, vol. 7, no. 4, pp. 041016-041016-9, Nov. 2015.

[26]   W. Thomson, *Theory of Vibration with Applications*. CRC Press, 1996.

[27]   dSPACE GmbH, "dSPACE_DS1104_Catalog2017_E.pdf." Rathenaustraße 26 33102 Paderborn, Germany, 2017.

[28] dSPACE GmbH, "dSPACE_ControlDesk_Product_information_07-2017_English_01_170719.pdf." Rathenaustraße 26 33102 Paderborn, Germany, 2017.

[29] Burr-brown Products from Texas Instrument, "High voltage-high current operational amplifier OPA 549." 2005.

[30] BEI Kimco, "voice-coil-actuator-linear-frameless-la30-48-000a.pdf." 1499 Poinsettia Avenue, Suite 160, Vista, CA 92081 USA, 2017.

[31] "What is a Voice Coil Actuator (VCA) – BEI Kimco Info." [Online]. Available: http://www.beikimco.com/resources-downloads/about-VCAs/what-is-a-voice-coil-actuator. [Accessed: 25-Jul-2017].

[32] Renishaw, "SiGNUM_encoder_system_data_sheet.pdf." Wotton-under-Edge, Gloucestershire, UK, 2017.

[33] Renishaw, "SiGNUM_software_users_guide.pdf." Wotton-under-Edge, Gloucestershire, UK, 2017.

[34] wegetit | wegetit.eu, "dsd anti vibration mounts." [Online]. Available: https://www.mecanocaucho.com/en-GB/products/anti-vibration-mounting/dsd-anti-vibration-mount/.

[35] F. Resta G. Diana, "Control of Mechanical System." [Online]. Available: https://www.scribd.com/document/313489039/Control-of-Mechanical-Systems. [Accessed: 25-Jul-2017].

[36] K. J. Åström and T. Hägglund, *Advanced PID Control*. ISA - The Instrumentation, Systems and Automation Society, 2006.

[37] R. D. Lorenz, J. J. Zik, and D. J. Sykora, "A direct-drive, robot parts, and tooling gripper with high-performance force feedback control," *IEEE Trans. Ind. Appl.*, vol. 27, no. 2, pp. 275–281, Mar. 1991.

[38] S. Y. Nof, *Handbook of Industrial Robotics*. John Wiley & Sons, 1999.

[39] R. D. Klafter, T. A. Chmielewski, and M. Negin, *Robotic engineering: an integrated approach*. Prentice Hall, 1989.

[40] M. Tiryakioglu, *Repeatability and Accuracy of an Industrial Robot: Laboratory Experience for a Design of Experiments Course*, vol. 9. 2009.

[41] Standard ISO 9283, "MANIPULATING INDUSTRIAL ROBOTS - PERFORMANCE CRITERIA & RELATED TEST METHODS." [Online]. Available: http://0-eu.i2.saiglobal.com.library.ucc.ie. [Accessed: 29-Jun-2017].

[42] C. T. Johnson and R. D. Lorenz, "Experimental identification of friction and its compensation in precise, position controlled mechanisms," *IEEE Trans. Ind. Appl.*, vol. 28, no. 6, pp. 1392–1398, Nov. 1992.